

Compositional Development as a Function of Spray Distance in Unshrouded/Shrouded Plasma-Sprayed $\text{Cr}_3\text{C}_2\text{-NiCr}$ Coatings

S. Matthews

(Submitted July 22, 2014; in revised form October 23, 2014)

Thermal spraying of $\text{Cr}_3\text{C}_2\text{-NiCr}$ composites generates varying degrees of carbide dissolution into the Ni binder. During high-temperature exposure, the carbide dissolution zones precipitate high concentrations of small carbides which develop into finely structured networks. This raises the possibility of producing unique tailored carbide composite structures through the generation of controlled carbide dissolution and appropriate heat treatment. The first step in this process is to produce a supersaturated Ni-Cr-C solid solution from which the carbide phase could be precipitated. In a previous work, a broad range of plasma parameters were trialed to assess their effect on the degree of carbide dissolution at a fixed spray distance of 100 mm. The current two-part work builds on the most promising plasma parameters from those trials. Part 2 of this article series investigated the effect of spray distance on the compositional development in $\text{Cr}_3\text{C}_2\text{-NiCr}$ coatings during high-energy plasma spraying. The coating compositions were analyzed in detail and quantified through Rietveld fitting of the coating XRD patterns. Coating microstructural features were correlated with the observed variations in composition. The effect of the spray parameters and spray distance on the equilibrium coating compositions is discussed.

Keywords amorphous Ni alloy, carbide dissolution, $\text{Cr}_3\text{C}_2\text{-NiCr}$, Cr_7C_3 , metastable $(\text{Cr,Ni})_7\text{C}_3$, shrouded plasma spray, spray distance

1. Introduction

Thermal spraying of $\text{Cr}_3\text{C}_2\text{-NiCr}$ coatings generates varying degrees of carbide dissolution into the Ni alloy binder. It is conventional practice to minimize such carbide dissolution to retain the highest carbide content possible, since high carbide content cermet coatings exhibit superior wear resistance (Ref 1-5). During high-temperature exposure, the zones of carbide dissolution precipitate high concentrations of small carbide grains which develop into finely structured and interconnected carbide networks (Ref 3, 5-7). The variation in these carbide structures that develop as a function of initial carbide dissolution, heat treatment temperature, and treatment time raises the possibility of tailoring the carbide phase morphology to exploit the beneficial wear resistance of submicron carbide grains, or the development of unique carbide composite structure functionalities.

The first step in exploring this concept for $\text{Cr}_3\text{C}_2\text{-NiCr}$ cermet coatings is the production of a coating with a supersaturated solid solution of Ni-Cr-C from which high concentrations of carbides could be precipitated with heat treatment. In a marked deviation from convention, the approach taken in this project to generate such coatings was to spray a conventional $\text{Cr}_3\text{C}_2\text{-NiCr}$ agglomerated and sintered powder under high-power plasma conditions. In a preliminary work, the effects of key plasma parameters (variations in nozzle geometry, Ar-He and Ar- H_2 plasma compositions, gas flow rates, and current) on the extent of carbide dissolution and carbon loss were characterized with and without shrouding at a spray distance of 100 mm (Ref 8). Shrouding was found to have a significant effect on the extent of carbide dissolution, oxide formation, carbon loss, and deposit efficiency of the $\text{Cr}_3\text{C}_2\text{-NiCr}$ coatings. The current work builds on these preliminary trials by analyzing in detail the effect of spray distance on the coating attributes sprayed under the most promising plasma parameter settings.

In Part one of this two-part article series, the effect of spray distance on the extent of carbide dissolution and carbon loss during high-energy plasma spraying of $\text{Cr}_3\text{C}_2\text{-NiCr}$ was analyzed (Ref 9). In this second of the two-part article series, the effect of spray distance on the compositional development in these coatings is discussed. The as-sprayed coatings compositions were analyzed in detail and quantified through Rietveld fitting of the coating XRD patterns. The coating microstructural features were correlated with the observed variations in composition. Heat treatment was used to transform the metastable as-sprayed coating composition toward equilibrium. The effect of the spray parameters and spray distance on the equilibrium coating compositions is presented.

S. Matthews, School of Engineering and Advanced Technology, Massey University, Private Bag 102904, Auckland 0745, New Zealand. Contact e-mail: s.matthews@massey.ac.nz.

1.1 Review of the Ni-Cr-C System

In conventional HVOF spraying of Cr₃C₂-NiCr coatings, the spray parameters are optimized such that the carbide and alloy components undergo as little interaction or degradation as possible. As such the coating phases tend to reflect those of the powder, with only minor changes. However, in this work, the aim was to dissolve as much of the carbide material into the Ni alloy as possible in-flight. Because the Ni, Cr, and C elements of the powder would be present in a mixed liquid phase, it would, in principle, be possible for any stable equilibrium composition of compounds or alloys to form from the combination of these elements. Furthermore, the rapid solidification of the molten splats upon impact raises the possibility of metastable phases also being present. In this section, the equilibrium and metastable phases formed by the combination of Ni, Cr, and/or C are reviewed. The key features of these phases relevant to this work are summarized in Table 1 (Ref 10-20).

1.1.1 Carbide Compounds. *Cr-C System:* The Cr-C equilibrium phase diagram indicates the formation of three stable carbide phases—Cr₃C₂, Cr₇C₃, and Cr₂₃C₆, all with narrow homogeneity ranges (Ref 20, 21). In the context of this Ni-Cr-C system, these carbides also show minimal solubility of Ni—5 at.% Ni in Cr₂₃C₆, 6 at.% in Cr₇C₃, and 0.7 at.% in Cr₃C₂ (Ref 19). The Ni solubility does not change significantly with temperature and has a negligible effect on the carbide lattice parameters due to the low Ni content and similarity in atomic radii of Cr and Ni (Ref 19). It is notable that the formation of Cr₂₃C₆ from the melt is readily suppressed through rapid cooling, leading to the formation of a metastable (Cr)+Cr₇C₃ eutectic (Ref 20). In a similar manner, Cr₃C₂ formation from the melt can also be suppressed by rapid solidification. During plasma spraying of blended Cr₃C₂-NiCr powder, the Cr₃C₂ powder particles melted to form a Cr-based liquid and graphite above 1813 °C (Ref 22). Rapid

Table 1 Review of phase information in the Ni-Cr-C System

| Compound/alloy | Information | References |
|---|--|--|
| | <i>Cr-C compounds</i> | |
| Cr ₃ C ₂ | Maximum Ni solubility = 0.7 at.% Crystal structure—orthorhombic Lattice parameters— $a = 0.5533$ nm, $b = 0.2829$ nm, $c = 1.147$ nm Unit cell volume = 0.180 nm ³ | Ref 19 Ref 12 Ref 12 Ref 12 |
| Cr ₇ C ₃ | Maximum Ni solubility = 6 at.% Crystal structure—orthorhombic Lattice parameters— $a = 0.4526$ nm, $b = 0.7010$ nm, $c = 1.2120$ nm Note: Several works have reported the crystal structure of Cr ₇ C ₃ as hexagonal or rhombohedral, but the orthorhombic structure has been confirmed in (Ref 20) | Ref 19 Ref 20 Ref 20 Ref 20 |
| Cr ₂₃ C ₆ | Maximum Ni solubility = 5 at.% Crystal structure—cubic Lattice parameters— $a = 1.064$ nm Unit cell volume = 1.205 nm ³ | Ref 19 Ref 12 Ref 12 Ref 12 |
| Cr ₃ C (metastable) | Crystal structure—orthorhombic Lattice parameters— $a = 0.458$ nm, $b = 0.512$ nm, $c = 0.680$ nm | Ref 12 Ref 12 |
| Cr ₅ C ₂ (metastable) | Crystal structure—Hagg carbide Fe ₅ C ₂ type structure | Ref 10 |
| Cr ₃ C _{2-γ} (metastable) | Crystal structure—filled Re ₃ B type structure | Ref 10, 14 |
| CrC _{1-z} (metastable) | Crystal structure—NaCl structure | Ref 10, 14 |
| Cr ₂ C (metastable) | Crystal structure—hexagonal | Ref 17 |
| | <i>Ni-C compounds</i> | |
| Ni ₃ C (metastable) | Crystal structure—hexagonal Lattice parameters— $a = 0.2631$ nm, $c = 0.4314$ nm Note: While several sources report a hexagonal crystal structure, Schaefer et al. (Ref 16) report that the true crystal structure is rhombohedral Note: The crystal structures of hcp-Ni and Ni ₃ C are almost identical | Ref 18 Ref 18 Ref 16 Ref 11, 18 |
| | <i>Ni- and Cr-based Alloys</i> | |
| Ni-C | Crystal structure of Ni—fcc Maximum equilibrium solubility of C in Ni = 2.7 at.% at 1326 °C | Ref 18 Ref 18 |
| Ni-Cr | Maximum metastable solid solubility of C in Ni = 7.4 at.% Maximum equilibrium solid solubility of Cr in Ni = 50 at.% Maximum metastable solid solubility of Cr in Ni = 62.8 at.% Ordered phase Ni ₂ Cr (Cr 25-36 at.%) (crystal structure—orthorhombic, MoPt ₂ type) | Ref 15 Ref 15 Ref 15 |
| Cr-C | Crystal structure of Cr—bcc Maximum equilibrium solid solubility of C in Cr = 0.3 at.% at 1534 °C | Ref 20 Ref 20 |
| Ni-Cr-C | Maximum solubility of C in (Ni) is ≈ 3 at.% C at 13.6 at.% Cr and decreases with further increase in Cr content Amorphous phase formation observed in Cr-Ni-C alloys at 27-51 at.% Ni and 15-23 at.% C. Critical cooling rate for amorphous phase formation ≈ 10^6 - 10^7 K/s | Ref 19 Ref 13 |

cooling upon impact prevented the reformation of Cr_3C_2 , leaving the graphite phase in the coating.

Several metastable chromium carbides have been reported. Inoue and Masumoto (Ref 12) reported the formation of metastable Cr_3C carbide formed during rapid quenching from Cr-C melts in the range $\text{Cr}_{78-87}\text{C}_{13-22}$. This compound remained unchanged at temperatures up to 700 °C, above which is transformed to a metastable Cr_7C_3 phase and finally to stable Cr_{23}C_6 . During crystallization studies of amorphous $\text{Cr}_{1-x}\text{C}_x$ alloys, Bouzy et al. (Ref 10) identified the formation of the following metastable chromium carbides as a function of the alloy carbon content: $X \leq 0.34$ — Cr_3C and Cr_5C_2 , $X > 0.34$ — $\text{Cr}_3\text{C}_{2-y}$ and CrC_{1-z} . The $\text{Cr}_3\text{C}_{2-y}$ metastable carbide has also been reported during the carbonization of chromium oxide (Ref 14). The metastable Cr_2C carbide has been observed to form during heating and reaction of C/Cr/C tri-layer films in Ref 17. These metastable phases have been observed at temperatures up to 650-700 °C (Ref 10, 17) above which they transform to equilibrium chromium carbides.

Ni-C System: There are no stable carbides in the Ni-C system (Ref 18). However, a metastable Ni_3C carbide has been identified during rapid splat quenching of Ni-C (Ref 23) and during heat treatment of mechanically alloyed Ni and carbon elemental powders (Ref 24). Differential scanning calorimetry trials on the mechanically milled powder indicated decomposition of the Ni_3C carbide into elemental Ni and graphite at 460 °C (Ref 24).

1.1.2 Alloy Compounds. Ni-Based Alloys: The Ni-C equilibrium phase diagram indicates a maximum solid solubility of C in fcc Ni of 2.7 at.% at 1326 °C. However, rapid solidification of Ni-C melts has been shown to form a highly supersaturated Ni fcc phase, along with the metastable Ni_3C carbide. According to the metastable phase diagram in Ref 18 the maximum metastable solid solubility of C in Ni is 7.4 at.%.

The Ni-Cr equilibrium phase diagram indicates a maximum solid solubility of Cr in fcc Ni of 50 at.% at 1345 °C (Ref 15). However, rapid solidification from the liquid phase has been reported to generate metastable extensions of Cr solid solubility up to 62.8 at.% (Ref 15). Increases in the Cr content generate an increase in the (Ni) alloy lattice parameters. The variation in the fcc lattice parameter, a_{Ni} , with Cr alloying ($X_{\text{Cr}} = \text{Cr mol fraction}$) has been modeled as Ref 25

$$a_{\text{Ni}}(\text{nm}) = 0.352 + 0.0178X_{\text{Cr}} - 5.97 \times 10^{-3}X_{\text{Cr}}^2,$$

A low-temperature (maximum temperature 590 °C) ordered phase at a composition of Ni_2Cr (Cr 25-36 at.%) is also reported in the equilibrium phase diagram (Ref 15). The formation of this phase is represented by a peritectic decomposition of the two-phase (Ni) and (Cr) structure to the ordered Ni_2Cr phase.

In the Ni-based ternary Ni-Cr-C system, the solid solubility of carbon is dependent upon the Cr content (Ref 19, 26). The maximum solubility of carbon in the Ni-based alloy reaches approximately 3 at.% at 13.6 at.% Cr, and decreases with higher Cr concentration (Ref 19). The maxi-

um C solubility in (Ni) occurs at the composition in equilibrium with Cr_3C_2 and graphite (Ref 26). At low concentrations of Cr, the lattice parameter of the fcc (Ni) alloy ternary solid solution is greater than the lattice parameter of binary solid solutions at an equivalent C concentration. With increasing Cr concentration, the difference between the ternary and binary solid solution lattice parameters decreases, indicating a reduction in the solubility of C in the (Ni) alloy with increasing Cr content (Ref 26).

Cr-Based Alloys: The Cr-C equilibrium phase diagram indicates a maximum solid solubility of C in bcc Cr of 0.3 at.% at 1534 °C (Ref 20). The carbon solubility in Cr in the Ni-Cr-C ternary system has not been widely investigated and is assumed to not exceed that of the Cr-C binary system (Ref 19, 26).

Several polymorphs of Cr have been proposed, but a detailed review by Nash (Ref 15) concluded that no conclusive evidence of polymorphic transformation in Cr exists and that Cr has a bcc structure up to its melting point. The Ni-Cr equilibrium phase diagram indicates a maximum solubility of Ni in bcc Cr of 32 at.% at 1345 °C (Ref 15). A low-temperature (up to approximately 600 °C) metastable σ phase has been proposed in binary Ni-Cr alloys at a composition of 71.8 at.% Cr.

Amorphous phase formation has been observed in Cr-Ni-C ternary alloys under rapid quenching conditions (Ref 13). In a $(\text{Cr-X})_{82}\text{C}_{18}$ alloy system, the formation of a completely amorphous phase occurred in the composition range $X = 27-51$ at.% Ni. More generally the carbon content in amorphous Cr-X-C based alloys, including $X = \text{Ni}$, was found to be limited to approximately 15-23 at.%. In the case of the Cr-Ni-C system, the addition of Ni appeared to reduce the critical cooling rate of amorphous phase formation (rate of $\approx 10^6-10^7$ K/s) relative to the Cr-C binary alloy (Ref 13).

2. Experimental Procedure

The coatings analyzed in Part 2 of this two-part article series were the same as those prepared for Part 1 (Ref 9). An agglomerated and sintered Cr_3C_2 -NiCr powder (H C Starck, Amperit 588 (H.C. Starck, Munich, Germany; nominal size $-45/+15 \mu\text{m}$) was sprayed onto degreased and grit-blasted mild steel substrates using a Praxair SG-100 plasma torch (Praxair Surface Technologies, Indianapolis, USA). A detailed description of the plasma spray set up and coating procedure is presented in Ref 8. Two plasma set ups were used—a high-velocity plasma set using a “Mach II” anode nozzle and a low-velocity plasma set using a “subsonic” anode nozzle, under the conditions of Table 2. For each plasma set up, all of the trials were sprayed in air (unshrouded trials) and then repeated using shrouding. The Mach II anode nozzle-shrouded trials were sprayed with a 90-mm-long solid conical coaxial copper shroud (Ref 9, 27). Argon shroud gas flowed through internal holes in the shroud wall at 3 SLPM and from a circular slot at the front of the shroud at 300 SLPM. Because of the length of this shroud, samples using the Mach II anode nozzle were only sprayed at 100 and

Table 2 Plasma spray parameters

| Trial number/description | Nozzle type | Shroud | Spray distance, mm | Ar flow (SLPM) | Secondary gas | Secondary flow (SLPM) | Carrier gas (SLPM) | Current, A | Power, kW |
|----------------------------------|-------------|--------------------|--------------------|----------------|----------------|-----------------------|--------------------|------------|-----------|
| CD01 Ar-H ₂ low flow | Mach II | No | 100, 120 | 50 | H ₂ | 5 | 2 | 600 | 30 |
| CD02 Ar-H ₂ high flow | Mach II | No | 100, 120 | 85 | H ₂ | 7 | 3 | 800 | 56 |
| CD03 Ar-H ₂ low flow | Mach II | Yes (solid shroud) | 100, 120 | 50 | H ₂ | 5 | 2 | 600 | 30 |
| CD04 Ar-H ₂ high flow | Mach II | Yes (solid shroud) | 100, 120 | 85 | H ₂ | 7 | 3 | 800 | 56 |
| CD05 Ar-He | Subsonic | No | 80, 100, 120 | 40 | He | 9 | 2.5 | 700 | 37.8 |
| CD06 Ar-H ₂ | Subsonic | No | 80, 100, 120 | 49 | H ₂ | 5 | 2 | 600 | 33 |
| CD07 Ar-He | Subsonic | Yes (gas shroud) | 80, 100, 120 | 40 | He | 9 | 2.5 | 700 | 37.8 |
| CD08 Ar-H ₂ | Subsonic | Yes (gas shroud) | 80, 100, 120 | 49 | H ₂ | 5 | 2 | 600 | 33 |

120 mm. The subsonic anode nozzle-shrouded trials used a shorter shroud segment to form a protective gas shroud (Ref 8, 9). Argon was fed to the shroud at 300 SLPM to form a 40-mm-diameter coaxial gas shroud around the plasma plume. The subsonic anode nozzle trials were sprayed at 80, 100, and 120 mm.

Coating samples cut from the sprayed substrates were mounted in cross section under vacuum in epoxy and metallographically prepared to a final 1 μm diamond polish. Scanning electron microscopy (SEM) (FEI, Oregon, USA) was used to analyze the cross-sectional images using back-scattered electron imaging (BSE). X-ray diffraction (XRD) (D2 Phaser fitted with a linear LYNX-EYE detector (5.83°, 192 channels)) (Bruker AXS GmbH, Karlsruhe, Germany) was used to characterize the composition of the coating surface. Patterns were measured in the angular 2θ range 20°–80° under the following operating parameters—Cu source ($\lambda = 1.541 \text{ \AA}$) at 30 kV and 10 mA, 0.02°/step, fixed divergence/anti-scattering slit 1 mm, primary and secondary axial Soller slit 2.5°, receiving slit 0.2 mm, Ni K β filter. Separate samples were cut from the bulk substrates and the coating surface ground and polished to a 3 μm diamond polish to remove any surface oxides and reduce the surface roughness prior to XRD analysis. Rietveld fitting of the XRD patterns was performed using the software package MAUD (Ref 28). Texture was not fitted in this analysis. It should be noted that the coating samples consisted of a complicated mixture of crystalline, semi-crystalline, and possibly amorphous phases, making quantitative analysis, a significant challenge. Therefore, the degree of fitting and quantification of the phase concentrations were not expected to reach “perfect” values. However, the intention of this preliminary analysis was to gain at least a first approximation of the variation in the relative amounts of the main coating phases as a function of processing parameters. Because of the complexity in the microstructure and phase distribution, this information could not be assessed by any other method.

Coating samples were heat treated in air at 800 °C for 3 h to enable the metastable and amorphous phases in the as-sprayed coatings to tend toward equilibrium. The heat-treated samples were ground and polished to a 3 μm diamond finish to remove the oxidized surface material prior to analysis. Rietveld fitting of the XRD patterns from these samples was again used to quantify the concentration of the coating phases.

3. Results and Discussion

3.1 Summary of the Main Conclusions from Part 1 (Ref 9)

Part 1 of this two-part article series characterized the effect of spray distance on the extent of carbide dissolution and carbon loss during spraying of the Cr₃C₂-NiCr coatings analyzed in this, the second part of this article series. In order to provide the background from the previous work and put the results of the current work in content, the main conclusions drawn from the first article are reviewed here.

In the unshrouded low flow rate Ar-H₂ Mach II anode nozzle trials (CD01), the increase in spray distance had only a minor effect on the degree of carbide dissolution (seen as a reduction in the carbide content), carbon loss, and deposit efficiency, Fig. 1 and 2. This was attributed to the high-particle velocities generated under these conditions which prevented significant reaction with the environment or phase transitions over this distance. At a spray distance of 100 mm, shrouding significantly increased the extent of carbide dissolution and deposit efficiency while reducing the degree of carbon loss relative to the unshrouded trial, Fig. 2. The high-particle velocity again resulted in no significant changes in the coating attributes with spray distance, aside from the degree of indicative carbon loss which increased from 100 to 120 mm.

The unshrouded high flow rate Ar-H₂ Mach II anode nozzle trials (CD02) at 100 mm were significantly influenced by non-optimal powder injection conditions which resulted in lower carbide dissolution but higher carbon loss relative to the lower flow rate trials, Fig. 2. The increase in spray distance to 120 mm did not significantly affect the coating properties. Shrouding overcame the powder injection conditions by enclosing all of the powder particles within the plasma plume. At a spray distance of 100 mm, shrouding dramatically decreased the coating carbide content through carbide dissolution and increased the deposit efficiency while also reducing the degree of indicative carbon loss. The increase in spray distance to 120 mm again led to an increase in the degree of carbon loss, but had a minimal effect on the other coating parameters. The increase in carbon loss with spray distance in the shrouded trials was attributed to the particles passing through a complex gas mixing zone outside the shroud where they were exposed to entrained oxygen prior to impact.

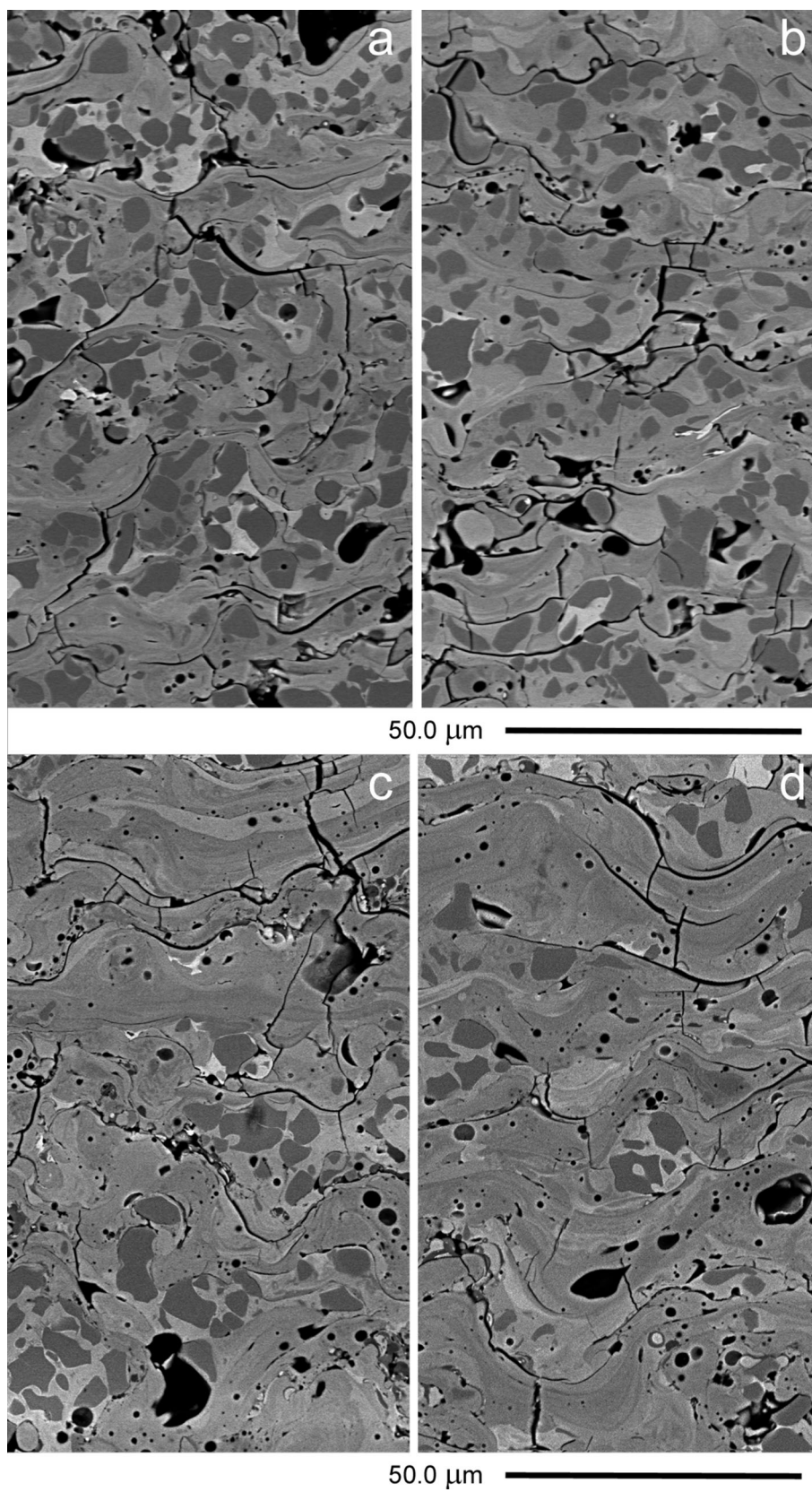


Fig. 1 Cross-sectional BSE images from the Mach II nozzle trials CD01 (a) and CD03 (b) at 100 mm, and the subsonic nozzle trails CD05 (c) and CD07 (d) at 80 mm spray distance

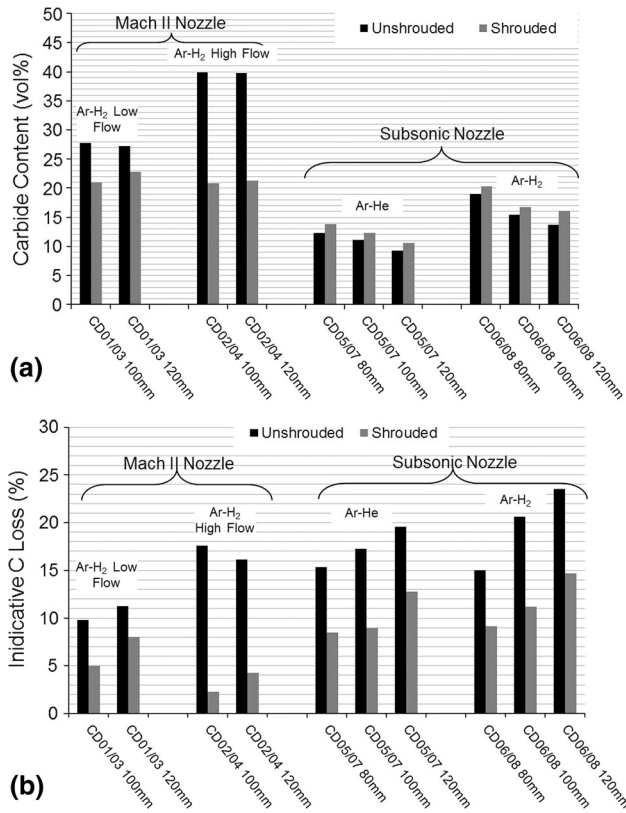


Fig. 2 Analysis of the coating properties for trials CD01-CD08 as a function of spray distance—carbide content (a) and indicative carbon loss (b)

In the unshrouded subsonic anode trials, increasing spray distance leads to a reduction in the coating carbide content and deposit efficiency but an increase in the degree of carbon loss, Fig. 1 and 2. Shrouding dramatically reduced the magnitude of carbon loss, but the degree of carbon loss still increased with increasing spray distance. There was a notable transition in the rate of carbon loss with shrouding which greatly increased beyond 100 mm. This was attributed to the combined effect of the particle trajectory moving away from the protective gas shroud and the increase in turbulent mixing and ambient air entrainment at longer distances. Unlike in the Mach II anode nozzle trials, shrouding did not lead to an increase in carbide dissolution (seen as a higher retained carbide content), which was attributed to cooling of the plasma by the cold shroud gas. The same trends were observed in both the Ar-He and Ar-H₂ trials, but the rates of variation in carbide dissolution and carbon loss were distinctly greater in the Ar-H₂ trials, Fig. 2.

3.2 Analysis of Phase Development with Carbide Dissolution—Phase Identification

The phases in the coatings were identified from XRD patterns by comparing the peaks in the pattern to reference patterns from pure materials from the JCPDS database and by fitting reference patterns to the XRD patterns using Rietveld analysis. As widely reported in the litera-

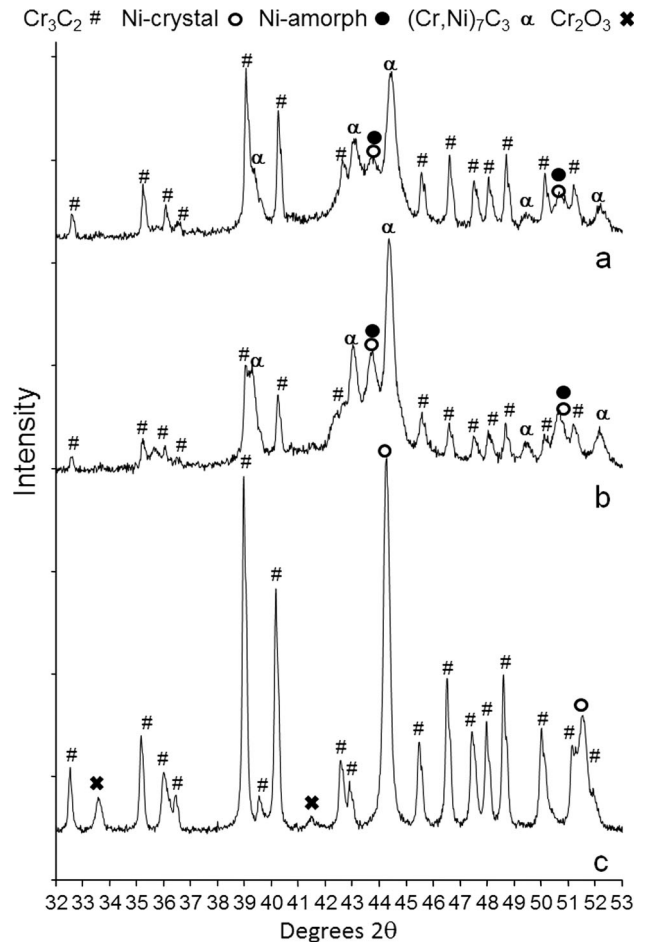


Fig. 3 XRD patterns for the as-sprayed coatings from trial CD01 at 100 mm (a) and CD07 at 120 mm (b), and the pattern after heat treatment for trial CD01 at 100 mm (c)

ture, the interpretation of XRD patterns from the Cr₃C₂-NiCr system is complicated by the overlap of peaks from the sub-carbides (Cr₇C₃ and Cr₂₃C₆) with those of the primary phases Cr₃C₂ and the Ni Alloy (Ref 5, 29). Furthermore, rapid solidification of the phases upon impact can lead to amorphous or nano-crystalline structures, resulting in variation in the crystal lattice dimensions and shifts in the peak positions (Ref 30). Figure 3(a) and (b) presents the XRD patterns for trials CD01 at 100 mm and CD07 at 120 mm which were representative of the low and high degrees of carbide dissolution (Note that trial CD02 had the lowest degree of carbide dissolution. However, it suffered a high degree of carbon loss. This apparently contradictory result was attributed to non-optimal powder injection conditions as discussed in Part 1 (Ref 9). The results of Trial CD01 were considered to be more representative of typical low carbide dissolution, low carbon loss coatings for this analysis). The XRD patterns for the remaining trials tended toward one or other of these patterns. Cr₃C₂ (JCPDS 35-0804) was readily identified by the presence of the two most intense peaks at 2θ = 39° and 40.2°, and the multiple smaller intensity peaks over the range 2θ = 45°-50°. The peaks of this compound did not

show any movement in peak position across all the trials irrespective of the degree of carbide dissolution. This is justified on the basis that these peaks result primarily from the Cr_3C_2 grains carried into the coating from the powder and, hence, did not melt in-flight and react with the molten Ni binder. In the Rietveld analysis, this phase was modeled using the COD database file 9009905 (Ref 31).

The Ni alloy material was assumed to form both a crystalline phase and a more dominant amorphous/nano-crystalline phase. The crystalline phase was assumed based on the relatively narrow and defined peak at approximately $2\theta = 43.8^\circ$ (JCPDS 04-0850). This phase was attributed to the Ni-rich regions in the partially molten splats. The intensity of this peak to the broad background beneath it varied significantly across the trials as a function of carbide dissolution. While the intensity of this peak appears to be significant in the raw pattern, it was found to be a relatively minor peak after Rietveld pattern fitting (Ni COD reference 9012427), Fig. 4(a). Because of the low concentration of this crystalline Ni alloy material, the most intense secondary peak was of very low intensity and overshadowed by peaks from the other phases in the region $2\theta = 51^\circ$. The peak positions of this phase were shifted to a lower 2θ position (higher d-spacing positions) relative to the crystalline Ni peaks in the starting powder due to the increase in Cr and C from carbide dissolution. The amorphous/nano-crystalline Ni alloy material was assumed to account for the large background features in the region $2\theta = 42^\circ$ - 45° and $2\theta = 50^\circ$ - 53° . For simplicity, this material will hereafter be referred to as the amorphous Ni alloy to avoid confusion with the previously defined crystalline Ni alloy material. However, it is understood that this amorphous material may exist as a nano-crystalline phase. Typically, Rietveld pattern fitting is only applied to well-defined crystalline peaks. However, because of the significant contribution of this amorphous Ni material to the coating composition, it was deemed necessary to account for it in the Rietveld analysis. Lutterotti (Ref 32) successfully applied the Rietveld analysis method to the quantification of amorphous silica glass in ceramic materials by approximating the amorphous phase as a nano-crystalline solid. The same approach was adopted here with the crystal structure information of the amorphous Ni alloy material approximated by that of pure Ni (Ni COD reference 9009862). During fitting of this amorphous peak using the MAUD software, the peak parameters were adjusted to approximate the broad peak shape and the software set to optimize the peak shape and position for crystal size and strain effects. The fitted peak for this phase enabled a suitable match to be made to the XRD pattern in the $2\theta = 42^\circ$ - 45° region but typically did not fit a broad lower intensity peak in the $2\theta = 50^\circ$ - 53° region. The reason for this is unknown and an area of focus for future work.

The formation of Cr_7C_3 was definitively indicated by the presence of secondary peaks of this phase—specifically the peak at $2\theta = 49.4^\circ$ which was independent of peaks from any of the other phases in this system, and the peak at $2\theta = 39.3^\circ$ which formed an obvious higher 2θ shoulder to the main Cr_3C_2 peak. The presence of other secondary peaks of significant relative intensity was evident in the coating XRD patterns, but analysis of these was compli-

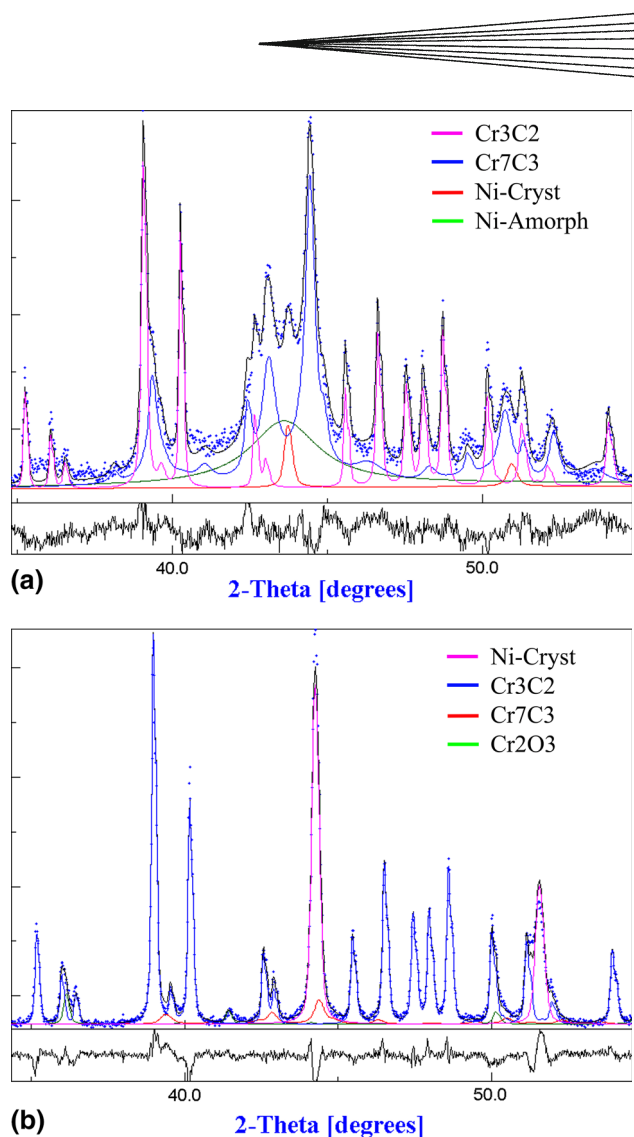


Fig. 4 Rietveld pattern fitting and residual plots over a subset of the analyzed 2θ range for the as-sprayed CD01 coating at 100 mm (a) and after heat treatment (b), showing the typical degree of fitting (Readers are referred to the on-line version of the article for the color image). The identified phases in image (a) were Cr_3C_2 —pink, Cr_7C_3 —blue, crystalline Ni alloy—red, and amorphous Ni alloy—green. The identified phases in image (b) were Cr_3C_2 —blue, Cr_7C_3 —red, crystalline Ni alloy—pink, and Cr_2O_3 —green

cated by overlap with peaks of other phases. The primary Cr_7C_3 peak was observed at approximately $2\theta = 44.4^\circ$. As with the other Cr_7C_3 peaks, this peak occurred at a higher 2θ position than that of the standard pattern (JCPDS 36-1482). This was attributed to substitution of smaller Ni atoms for Cr atoms in the Cr_7C_3 structure to form a metastable $(\text{Cr,Ni})_7\text{C}_3$ phase, hereafter referred to as “metastable Cr_7C_3 .” While Cr_7C_3 may dissolve up to 6 at.% Ni at equilibrium, the phase in this work is postulated to exhibit significant extension of Ni solubility due to rapid solidification. Analysis of this peak was complicated by its high relative intensity to the other metastable Cr_7C_3 peaks in the XRD pattern. Initially this was thought to result from the presence of a Ni alloy, a Cr-based alloy

(JCPDS 06-6941), and/or Cr_{23}C_6 (JCPDS 35-0783), the most intense peaks of which all occur close to that of the main metastable Cr_7C_3 peak, Fig. 5. However, all of these phases were eliminated upon further analysis. An Ni alloy in this peak position was discounted because this peak was equivalent or at a higher 2θ position than in the starting powder. This implies either no Cr dissolution into the Ni alloy or in fact a lower Cr content than in the starting powder. Both scenarios were considered unlikely, or to represent a very small concentration of material which would not account for the intensity of the observed peak. In addition, no secondary peaks were found to match this proposed primary Ni peak. The formation of a Cr-based alloy phase may in principle occur in regions where the carbide grains melted to form a Cr alloy and graphite, and which solidified fast enough to prevent carbide reformation. However, closer examination of the main bcc Cr peak showed that it was at a slightly higher 2θ position than the main metastable Cr_7C_3 peak. For this phase to contribute to the metastable Cr_7C_3 peak, it would require a shift in the 2θ position to a lower value, which implies an increase in d-spacing. Alloying with Ni would shift the Cr peaks to a lower d-spacing (higher 2θ position) (Ref 15) due to the smaller size of the Ni atom. Therefore, a shift to a higher d-spacing could only occur if there was significant interstitial C alloying, which is justifiable in principle. However, no secondary Cr peak was observed in the XRD pattern. Furthermore, no graphite peaks were observed either which would have been expected to form according to the proposed carbide melting mechanism (Ref 22). Therefore, if a Cr alloy does contribute to the formation of the main metastable Cr_7C_3 peak, its concentration is assumed to be very low. The main peak in the pattern of pure Cr_{23}C_6 occurs at a lower 2θ position than the proposed metastable Cr_7C_3 peak in this work, but a potential shift in peak position is justifiable due to Ni dissolution in the structure. However, the presence of significant quantities of this compound was discounted on the basis that no secondary peaks were observed in the coating XRD patterns. In addition, it has been previously reported that Cr_{23}C_6 formation is often suppressed under rapid solidi-

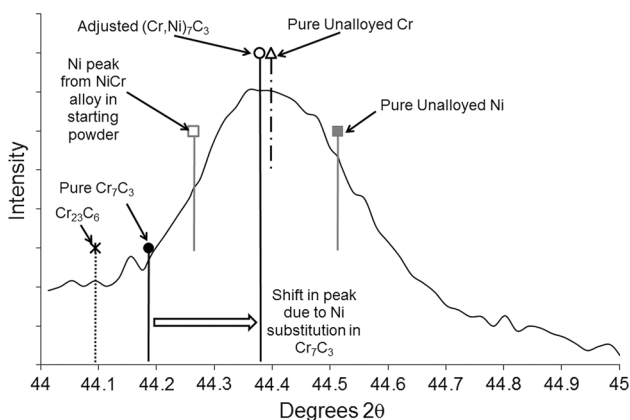


Fig. 5 Schematic indicating the peak positions of possible alloys and compounds in the region of the most intense peak in the coating XRD patterns

fication such as that experienced in this work. While such a qualitative analysis cannot totally discount these additional phases from being present in the coating, it does suggest that if they form, their concentration is very low. The complication regarding the high metastable Cr_7C_3 peak intensity at $2\theta=44.4^\circ$ was resolved following the Rietveld fitting of the coating XRD pattern, where it could be seen that the broad amorphous Ni phase peak contributed significantly to the observed peak intensity, Fig. 4(a). While several other phases could have potentially formed, as noted in the review of the Ni-Cr-C system in the introduction, none of these phases was definitively identified from the XRD patterns across the range of coatings investigated.

The dominance of the proposed metastable Cr_7C_3 phase peaks in the XRD patterns did not match the BSE cross-sectional images where the only carbides seen were those of Cr_3C_2 retained in the partially molten splats. To confirm if the proposed metastable Cr_7C_3 phase was a stable equilibrium compound or a metastable phase formed as a result of rapid solidification, the samples were heat treated at 800°C for 3 h in air to enable the equilibrium composition to develop. The XRD patterns of the heat-treated coatings were dominated by narrow crystalline peaks from Cr_3C_2 and the Ni alloy, with low intensity but definitive peaks from Cr_2O_3 , Fig. 3(c). No broad background peaks indicative of amorphous material were seen. Evidence for the presence of metastable Cr_7C_3 was dramatically reduced relative to the as-sprayed XRD patterns and was complicated by overlap of the primary Ni alloy and Cr_3C_2 peaks. Rietveld fitting of the heat-treated XRD patterns was used to quantify the metastable Cr_7C_3 concentration, Fig. 4(b). The dominance of the metastable Cr_7C_3 phase in the as-sprayed coating and its dramatic reduction in concentration in the equilibrium coating composition following heat treatment indicates that this was a metastable phase in the as-sprayed coatings.

During spraying, the carbide grains dissolve into the molten Ni binder, or melt themselves. Mixing of the elemental compositions in the liquid phase generates a Ni-Cr-C solution, which undergoes rapid solidification upon impact. If only minimal carbon loss occurs in-flight, the overall composition of this mixture would approximate the elemental composition of the starting powder—Ni 12.9 at.%, Cr 52.6 at.%, and C 34.5 at.%. The rapid solidification studies highlighted in the introduction section for Ni-C and Cr-C systems indicate that neither of these alloy systems could account for the large amount of carbon in this mixture. However, since no graphite peak was observed in any of the coating XRD patterns, this implies that a separate carbon phase did not form to an appreciable extent, and that the carbon must have been accommodated within the Ni-Cr-C solution in some way. Based on the results of this work, it is postulated that the rapid solidification of the Ni-Cr C solution generated a metastable supersaturated solid with an orthorhombic structure that approximated that of Cr_7C_3 . In terms of the solution composition, this hypothesis is supported by the fact that the elemental composition approximates the form $(\text{Cr,Ni})_7\text{C}_3$.

3.3 Phase Development in the As-Sprayed Coatings

Table 3 summarizes the weight percent concentrations of the coating phases, along with the goodness-of-fit (GoF) parameters from the Rietveld fitting using the MAUD software. Errors are presented for the parameters that were refined by the software program. The results are presented in graphical form in Fig. 6 and 7.

3.3.1 Mach II Ar-H₂ Trials. Low Flow Rate Trials—Unshrouded (CD01) and Shrouded (CD03): The Cr₃C₂ content decreased with the use of shrouding, indicating an increase in the extent of carbide dissolution, Fig. 6. This trend matched that discussed from the image analysis of the carbide content in Part 1 (Ref 9) and in this instance, the concentration of this phase was also comparable, Fig. 2. The metastable Cr₇C₃ phase dominated the coating composition in both the unshrouded and shrouded trials. The high concentration of this phase indicates that the majority of the mid-gray contrast “dissolution zone” material must have been made up of this material, more so than the amorphous Ni alloy. Conceptually, this is logical in that the Ni content was only 19.4 wt.% in the starting powder and could not, therefore, account for the large volume of mid-gray material present in the BSE images. The metastable Cr₇C₃ concentration was comparable in both unshrouded and shrouded coatings but showed contrasting trends with spray distance. At 100 mm, a greater amount of amorphous Ni alloy was formed in the shrouded coating compared to the unshrouded coating, but at 120 mm, the results were comparable. The variation in this phase with spray distance was complicated by the variation in the metastable Cr₇C₃ content. The crystalline Ni alloy content was low in both the unshrouded and shrouded trials and showed only minor change with spray distance. As this phase was

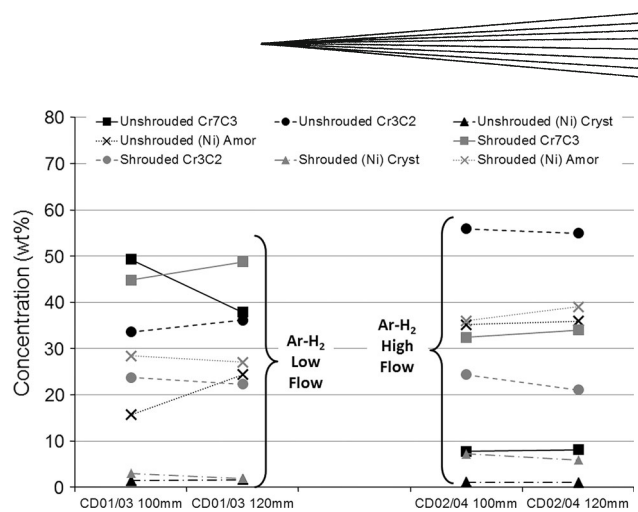


Fig. 6 Variation in the as-sprayed coating composition as a function of spray distance for the unshrouded and shrouded Mach II nozzle trials CD01-CD04

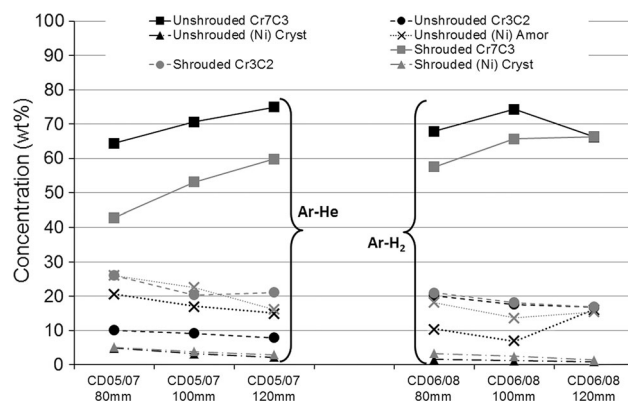


Fig. 7 Variation in the as-sprayed coating composition as a function of spray distance for the unshrouded and shrouded subsonic nozzle trials CD05-CD08

Table 3 Results from the Rietveld analysis for the As-sprayed coatings

| Trial number/description | Spray distance, mm | Concentration (wt.%) | | | | R value Rw (%) | Goff (sigma) |
|----------------------------------|--------------------|----------------------|-------------|--------------------------------|--------------------------------|----------------|--------------|
| | | Ni (Cryst) | Ni (Amorph) | Cr ₃ C ₂ | Cr ₇ C ₃ | | |
| CD01 Ar-H ₂ low flow | 100 | 1.4 | 15.7 (±1.1) | 33.6 (±2.0) | 49.3 (±2.9) | 3.49 | 1.47 |
| | 120 | 1.6 | 24.3 (±1.5) | 36.2 (±2.1) | 37.9 (±2.2) | 3.82 | 1.61 |
| CD02 Ar-H ₂ high flow | 100 | 1.1 | 35.2 (±3.5) | 55.9 (±5.4) | 7.8 (±1.0) | 3.32 | 1.45 |
| | 120 | 1.0 | 35.9 (±3.4) | 55.0 (±5.1) | 8.1 (±1.0) | 3.24 | 1.46 |
| CD03 Ar-H ₂ low flow | 100 | 3.0 | 28.4 (±1.5) | 23.7 (±1.1) | 44.8 (±2.0) | 4.18 | 1.70 |
| | 120 | 1.9 | 27.0 (±1.2) | 22.3 (±0.9) | 48.8 (±2.0) | 3.64 | 1.51 |
| CD04 Ar-H ₂ high flow | 100 | 7.2 | 35.9 (±1.6) | 24.4 (±1.1) | 32.4 (±2.4) | 6.11 | 2.49 |
| | 120 | 5.9 | 39.1 (±2.9) | 21.0 (±1.1) | 34.0 (±1.4) | 5.46 | 2.27 |
| CD05 Ar-He | 80 | 4.9 | 20.6 (±1.1) | 10.1 (±0.6) | 64.4 (±2.2) | 5.75 | 2.42 |
| | 100 | 3.2 | 17.0 (±1.3) | 9.1 (±1.0) | 70.6 (±3.0) | 5.03 | 2.07 |
| | 120 | 2.2 | 14.9 (±1.3) | 7.9 (±0.7) | 74.9 (±4.4) | 5.29 | 2.21 |
| CD06 Ar-H ₂ | 80 | 1.6 | 10.3 (±0.8) | 20.2 (±1.2) | 67.9 (±3.5) | 4.06 | 1.66 |
| | 100 | 1.2 | 6.9 (±1.0) | 17.6 (±1.4) | 74.3 (±5.6) | 4.01 | 1.62 |
| | 120 | 1.0 | 16.0 (±2.0) | 16.7 (±2.0) | 66.3 (±7.5) | 3.90 | 1.58 |
| CD07 Ar-He | 80 | 5.1 | 26.1 (±1.4) | 26.0 (±1.1) | 42.7 (±1.5) | 4.95 | 2.04 |
| | 100 | 3.9 | 22.6 (±1.0) | 20.4 (±1.0) | 53.2 (±1.8) | 4.55 | 1.87 |
| | 120 | 2.9 | 16.2 (±0.8) | 21.1 (±0.8) | 59.8 (±2.0) | 4.20 | 1.74 |
| CD08 Ar-H ₂ | 80 | 3.3 | 18.1 (±1.0) | 21.0 (±0.7) | 57.6 (±1.6) | 4.15 | 1.71 |
| | 100 | 2.4 | 13.6 (±1.0) | 18.2 (±1.0) | 65.7 (±2.6) | 4.25 | 1.73 |
| | 120 | 1.3 | 15.4 (±1.3) | 16.9 (±1.1) | 66.3 (±4.2) | 3.68 | 1.5 |

assumed to represent the Ni-rich alloy in partially molten splats, it implies that little of this material was present, and its concentration did not vary significantly as a function of spray distance.

High Flow Rate Trials—Unshrouded (CD02) and Shrouded (CD04): The unshrouded trial retained the highest Cr_3C_2 content of all the trials, implying the lowest degree of carbide dissolution, Fig. 6. The amorphous Ni alloy content was significantly higher in concentration than the metastable Cr_7C_3 phase. The concentration of approximately 35–38 wt.% was more than double the Ni alloy content in the starting powder of 15 wt.% based on the Rietveld analysis of the powder XRD pattern. This result implies that with low degrees of carbide dissolution, the dissolved Cr and C atoms are largely accommodated within the Ni alloy to form a supersaturated Ni-Cr-C solid solution with an amorphous/nano-crystalline structure. The low metastable Cr_7C_3 content suggests that the Ni-Cr-C liquid phase preferentially forms the amorphous Ni alloy upon solidification, with the metastable Cr_7C_3 phase only forming if there is an excess of Cr and C that cannot be entrained in the Ni solid solution.

Shrouding leads to a dramatic decrease in the Cr_3C_2 content under these plasma conditions, to a level comparable with that of the low flow rate trials, Fig. 6. This result showed a strong correlation with the carbide content results from image analysis in both the trend and relative magnitude between the unshrouded and shrouded coatings, Fig. 2. The differences in the quantitative results from each analysis method arise because the image analysis results only account for carbides greater than 1 μm in diameter, whereas the XRD results are generated from all of the Cr_3C_2 material within the analysis volume. The amorphous Ni alloy content remained comparable to that in the unshrouded coating. The excess Cr and C generated by the increased carbide dissolution lead to a dramatic increase in the metastable Cr_7C_3 content. The concentrations of each phase were comparable at both 100 and 120 mm, indicating that the physical state of the particle did not change significantly over this range under these high-velocity conditions.

It is notable that in the shrouded trials, both the low flow rate and high flow rate trials generated comparable levels of carbide dissolution based on the reduction in Cr_3C_2 content. However, the high flow rate trial coatings had a higher amorphous Ni alloy content and lower metastable Cr_7C_3 content compared to the coatings produced under the low flow rate conditions. This implies that the particle velocity played a role in the phase distribution for a given degree of carbide dissolution. However, the mechanism to account for this effect is unknown.

3.3.2 Subsonic Trials—Ar-He (CD05 and CD07) and Ar-H₂ (CD06 and CD08). In the Ar-He trials, the Cr_3C_2 content was higher in the shrouded trial relative to the unshrouded trial, Fig. 7, with the variation in composition significantly greater than that indicated in the image analysis results, Fig. 2. In contrast, the Cr_3C_2 content was comparable in both the unshrouded and shrouded Ar-H₂

trials. In all cases, the Cr_3C_2 content decreased with increasing spray distance, indicative of increasing carbide dissolution with the longer exposure time in the plasma.

The amorphous Ni alloy content was consistently lower in the unshrouded trials for both plasma compositions. In most cases, the contribution of this phase decreased with increasing spray distance. It is significant to note that the amorphous Ni concentration in these trials was lower than in the Mach II anode nozzle trials and close to the 15 wt.% Ni alloy content in the starting powder.

The metastable Cr_7C_3 phase dominated the composition in all the subsonic anode nozzle coatings. The rise in concentration of this phase with increasing spray distance correlated with the reduction in Cr_3C_2 content. The unshrouded trials formed consistently higher concentrations of metastable Cr_7C_3 than the shrouded trials for both plasma compositions. The concentration of this phase was significantly higher than in the Mach II anode nozzle trials, presumably due to the greater degree of carbide dissolution.

In general, the results from the subsonic trials support the mechanism of phase development proposed above—with increasing carbide dissolution, the molten Ni alloy becomes increasingly enriched in Cr and C. Upon solidification, the supersaturated Ni alloy cannot accommodate all the Cr and C in solution, and the excess amounts of these elements form the metastable Cr_7C_3 phase. Since the quantity of dissolved carbide greatly exceeds that of the Ni alloy at high degrees of carbide dissolution, the metastable Cr_7C_3 phase increasingly dominates the coating composition.

3.3.3 Analysis of the Amorphous Ni Alloy Phase Composition. In the mechanism proposed above, the liquid phase containing the Ni alloy and dissolved carbide elements preferentially forms a supersaturated Ni alloy, with the excess Cr and C elements forming the additional metastable Cr_7C_3 phase. If this occurs, it would follow that the amorphous Ni phase should have a comparable Cr and C concentration across all of the samples. To test this hypothesis, the unit cell dimensions of the amorphous Ni phase were calculated from the peak position in the Rietveld analysis using the MAUD software package. The Cr content of this Ni alloy was calculated using the correlation in (Ref 25), which assumes that Cr is the only alloying element. It is acknowledged that this is a weak assumption because carbon dissolved in the solid solution would also contribute to the variation in unit cell dimensions. However, no mathematical correlation could be found in the literature to describe the variation in Ni lattice parameter as a function of both Cr and C. These results then serve as a qualitative first attempt at comparing the composition of this amorphous/nano-crystalline phase. Figure 8 presents the calculated Cr wt.% concentration in the amorphous/nano-crystalline Ni alloy for both the Mach II and subsonic anode trials. In the subsonic anode nozzle trials, the average result for each parameter setting fell in the range 45–50 wt.% Cr. Similarly, in the Mach II anode nozzle trials, both the unshrouded coating results fell in this range. The shrouded Mach II anode results were significantly higher than this composition. However,

the reasons for this are unclear. This composition range is significant in that it equates to the maximum equilibrium solubility of Cr in Ni of approximately 47 wt.%. These comparable Ni alloy Cr concentrations occurred across samples which exhibited significant variation in coating composition, particularly in the metastable Cr_7C_3 concentration. This result, therefore, provides some support for the mechanism proposed above.

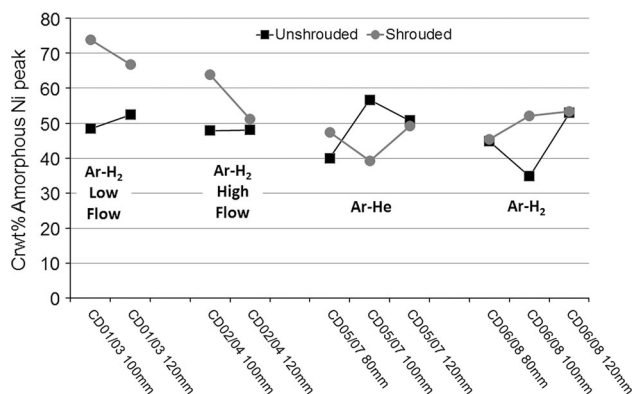


Fig. 8 Variation in the Cr concentration in the amorphous Ni alloy phase in the as-sprayed coatings from trials CD01-CD08 as a function of spray distance

3.4 Microstructure Development

3.4.1 Carbide Morphology. The XRD analysis indicated that the coating compositions were dominated by Cr_3C_2 , metastable Cr_7C_3 and amorphous Ni phases, with minor amounts of crystalline Ni alloy. The Cr_3C_2 carbide was assumed to result primarily from the large carbide grains retained from the starting powder. These were typically isolated individual grains and showed rounded morphologies indicative of having undergone dissolution into the molten Ni alloy, Fig. 9(a). In some instances, the carbide morphology was elongated as if it had flowed, suggesting that the grains had reached the point of melting.

Carbide precipitation from the supersaturated Ni matrix formed several distinct morphologies as a function of particle cooling. In splats where carbide grains were retained from the powder, large acicular carbide crystals were often observed, Fig. 9(b). Their elongated needle-like morphology indicated that growth was favored in one crystallographic direction. They were typically isolated, individual crystals that were oriented randomly with regard to the splat. This implied that their growth was not directed in one direction due to thermal flow as is typically observed in splat solidification (Ref 33). These characteristics indicate that these precipitates most likely formed in the liquid Ni alloy matrix prior to impact and solidifi-

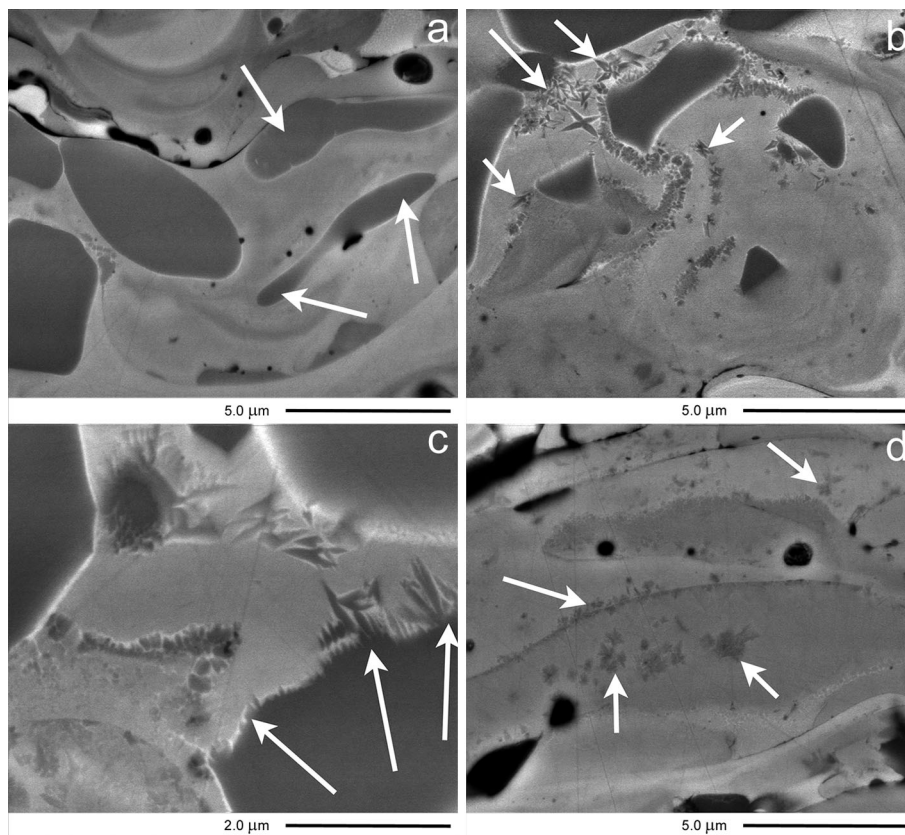


Fig. 9 Cross-sectional BSE images illustrating different carbide morphologies in the as-sprayed coatings—rounded carbides (a), acicular carbide precipitates (b), preferential carbide growth on retained carbide grains (c), and isolated carbide precipitates within high carbide dissolution zones (d)

cation. Their large size and preferential growth direction imply that they formed over a significant period, meaning that they must have begun to form soon after injection into the plasma. Furthermore, their formation implies that the molten Ni matrix was cooling over this time, otherwise their small size and high surface area would favor their preferential dissolution. The formation of these precipitates indicates that the powder particles were rapidly heated after injection into the plasma in order to melt the Ni alloy binder and generate significant carbide dissolution. The powder particles reached their peak temperature at a short-distance downstream and then began to cool. Precipitation of the carbide indicates that the particle temperature either did not reach, or quickly cooled below the melting temperature of Cr_3C_2 ($T_{\text{MELT}} = 1811\text{ }^\circ\text{C}$ (Ref 20)) or Cr_7C_3 ($T_{\text{MELT}} = 1766\text{ }^\circ\text{C}$ (Ref 20)), while the deformed nature of the splats containing these precipitated indicates that they remained at temperatures greater than the Ni-Cr melting temperature of $1345\text{--}1455\text{ }^\circ\text{C}$ (Ref 15). As the particle temperature decreased, the solubility of Cr and C in the liquid Ni alloy decreased. This is indicated somewhat by the step liquidus line on the Cr-rich side of the Ni-Cr phase diagram (Ref 15). The excess Cr and C rejected from the solution would support carbide precipitation.

While Cr_3C_2 grains were retained in the particle during such slow cooling in-flight, preferential carbide precipitation occurred on the surface of the grains, Fig. 9(c). Precipitation appeared to occur on the regions of most favorable crystallographic orientation based on the morphology of the precipitates and grew out into the supersaturated Ni Alloy. The size of such features indicates that they developed over an extended period of time. Typically such precipitates were surrounded by a bright contrast zone. Carbide formation occurred by diffusion of Cr and C out of the Ni supersaturated solution, creating a localized zone richer in Ni and poorer in Cr and C. The bright contrast is the result of the higher atomic mass of this Ni-rich material surrounding the low atomic mass, dark contrast carbide. These carbide precipitate morphologies were typically observed in splats in which high concentrations of Cr_3C_2 particles were retained from the powder. They were more common in the Mach II anode trials than in the subsonic trials. They were most likely formed by particles which passed through the plasma hot zone initially, but then traveled primarily along the colder plasma plume periphery. This not only would account for this rapid initial melting, but also the longer duration at lower temperatures over the majority of their flight required for elongated growth. It is notable that preferential carbide precipitation did not occur on all of the retained carbides to the extent indicated in Fig. 9(c). This indicates that such preferential nucleation and growth only occurred under specific conditions which were not widely met by many of the retained carbides. In a lot of instances, carbide precipitation on the retained Cr_3C_2 carbides appeared to be subtle. It was seen in the development of small nodules on the carbide periphery or implied through the appearance of a thin-bright contrast band of Ni-rich material around the outside of retained carbide grains, Fig. 9(c). The thin submicron thickness of the Ni-rich bands indicates the

short diffusion path of the precipitating Cr and C elements. This suggests that precipitation by this mechanism may have occurred rapidly during impact and splat solidification.

Carbide precipitation was also commonly observed in the subsonic anode nozzle coatings where there were few, if any, retained Cr_3C_2 grains, Fig. 9(d). These precipitates typically occurred as isolated features within the high Cr and C content dissolution zones. They were a lot smaller in size than those seen in the Mach II trials but showed similar acicular grain growth in the preferential crystallographic orientations. Such features are again indicative of carbide precipitation and growth within the molten Ni alloy matrix. Their small size means that they grew over a shorter period of time, suggesting that the particle cooled below the carbide melting temperature for only a short time before impact.

The composition of the precipitated carbides could not be confirmed with the analytical methods used in this work. Where precipitation occurred on the surface of retained Cr_3C_2 carbides, it is possible that either Cr_3C_2 or Cr_7C_3 formed. Both carbides have orthorhombic crystal structures. However, there is a significant difference in the lattice parameters between the two phases (Ref 20) which would favor preferential Cr_3C_2 precipitation over that of Cr_7C_3 . The grayscale contrast of the precipitates was comparable to the larger retained Cr_3C_2 grains, supporting this hypothesis. However, Cr_3C_2 precipitation requires significant quantities of Cr and particularly C to be present. If significant carbide diffusion away from the dissolved carbides occurred during the carbide dissolution period, then this would inhibit the ability of Cr_3C_2 to form and favor Cr_7C_3 . The morphology of the carbide precipitates suggests that they were crystalline and, therefore, detectable by XRD. However, the relatively low concentration of these precipitates means that any contribution they may have made to the carbide XRD peaks would have been overshadowed by the dominant Cr_3C_2 peaks from the retained carbides or the metastable Cr_7C_3 phase peaks. Further analysis by TEM is required to determine the precipitate composition. However, such an analysis is complicated by the extreme heterogeneity of the coating microstructure and isolated nature of the precipitates relative to the TEM analysis area.

3.4.2 Splat Boundary Carbide Formation. A notable feature, particularly in the subsonic anode nozzle trials, was the formation of a thin band of carbide grains along the splat boundaries, Fig. 10. While not seen in every splat, such features were common throughout the coating. While the carbides formed at the top of a splat, it is postulated that the heat from the solidifying splat above was sufficient to reheat the underlying splat and generated conditions under which sufficient Cr and C diffusion could occur to form the carbide grains. Diffusion of these elements, or at least diffusion of carbon, is implied by the presence in this zone of bright contrast material below the precipitated carbides. This is thought to represent high-atomic mass Ni-rich material left behind by the diffusion of the carbide forming elements to the splat interface. While carbides formed at the base of the splat, Fig. 10(a),

it is postulated that the grain structure in the solidified splat below provided a preferential site for carbide precipitation to occur from the supersaturated Ni alloy during splat spreading and solidification. The carbides were typically orientated perpendicular to the splat boundary in the direction of heat flow during splat solidification.

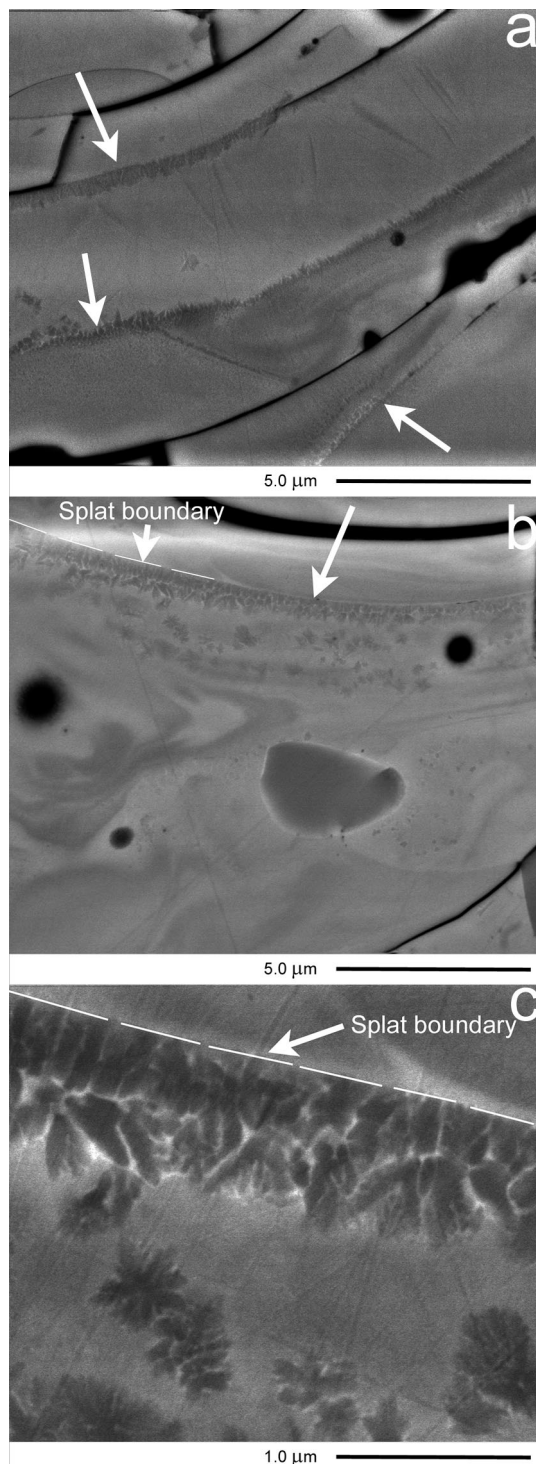


Fig. 10 Cross-sectional BSE images highlighting splat boundary carbide precipitation

3.4.3 Microstructure of the Amorphous Ni Alloy and Metastable Cr_7C_3 Phase. The microstructure of all the coatings in the BSE images was dominated by the mid-gray carbide dissolution zones of varying grayscale contrast between that of the bright contrast original Ni alloy and of the darker contrast Cr_3C_2 grains. These mid-gray zones must, therefore, account for the amorphous Ni alloy and metastable Cr_7C_3 phases which dominated the as-sprayed coating compositions. The variation in grayscale reflects the variation in the Cr and carbon concentrations both between and within the splats. Initially, the Ni alloy matrix melts, and carbide dissolution begins. During this period, the Ni alloy becomes increasingly saturated with dissolved Cr and C. As the particle temperature increases, the rate of carbide dissolution increases, along with the solubility of Cr and C in the Ni alloy. The high number of particles exhibiting total carbide dissolution suggests that in many cases, the particle temperature exceeded the melting temperature of Cr_3C_2 at some point. By this time, the Ni alloy is potentially saturated with dissolved Cr and C, which would inhibit diffusion of these elements from the molten carbide zones due to the reduced concentration profiles. Cooling of the particle in-flight reduces the solubility of Cr and C in the Ni alloy, further reducing inter-diffusion between the different concentration zones within the molten particles. Under such conditions, significant compositional heterogeneity may be retained in the molten particle. This is postulated to account for the formation of the dark contrast “swirl” features seen within the majority of the splats in which significant carbide dissolution had occurred in-flight, Fig. 11.

The retention of the mid-gray carbide dissolution zones in the coating splats indicates that the particles were at a high temperature at the point of impact and underwent rapid solidification. The results of the XRD analysis indicate that during solidification, the Ni-Cr-C solution forms a two-phase mixture consisting of an amorphous Ni alloy supersaturated in Cr and C, and a metastable Cr- and

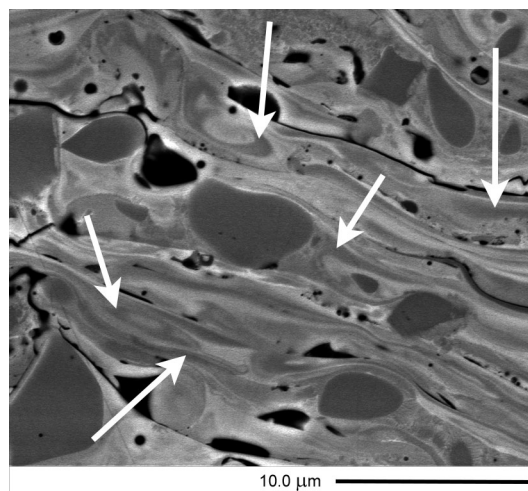


Fig. 11 Cross-sectional BSE image illustrating the dark contrast “swirl” features in splats in which high degrees of carbide dissolution occurred

C-rich phase with a structure approaching that of $(\text{Cr,Ni})_7\text{C}_3$. The relative amounts of each phase are dependent upon the local composition—areas of low carbide dissolution or low carbon concentration would form more of the amorphous Ni alloy, while zones of high carbide dissolution and high retained carbon content would form more of the metastable Cr_7C_3 phase. High-magnification BSE images revealed the formation of two distinct phases within the “carbide dissolution” zones, Fig. 12. These images were captured by imaging the same area at a high scan rate and averaging the information collected over a period of more than 60 s (given the location, morphology, and presence of localized bright-contrast high-atomic mass material within these features, they are not believed to have results from surface-based carbon contamination). Image analysis software was used to adjust the grayscale range of the images to enhance the subtle features in the image. Zones that appeared to be of homogeneous grayscale contrast at low magnification were shown at high magnification to have localized grayscale variation at a sub-100 nm scale, implying localized variation in atomic mass. The darker contrast features are assumed to be richer in Cr and C and account for the metastable Cr_7C_3 . The brighter contrast surrounding matrix is assumed to be the higher atomic mass amorphous/nano-crystalline-supersaturated Ni alloy phase. Additional analysis using transmission electron microscopy is required to confirm the proposed compositions of these phases.

The mechanism by which the supersaturated Ni-Cr-C liquid separates into these two phases upon rapid solidification is unknown. The similarity in the Ni alloy composition across the different as-sprayed coatings suggests that solidification of this phase with the maximum concentration of Cr and C in metastable solid solution forced the excess Cr and C atoms to clump together and form the metastable Cr_7C_3 . If the transformation of the Ni-Cr-C solution into two phases was driven by metastable carbide precipitation, then Ni alloy phase would be expected to show a greater variation in composition as a function of the extent of carbide dissolution in the coating. However, the melting point of Cr_7C_3 and presumably also $(\text{Cr,Ni})_7\text{C}_3$, is notably higher than that of the Ni alloy which would support the initial solidification of the metastable carbide prior to that of the Ni alloy. Such analysis is complicated by the lack of data relating to the metastable $(\text{Cr,Ni})_7\text{C}_3$ phase. Furthermore, the mechanism of phase formation is also thought to be dependent upon the local composition and the heat flow and rate of cooling through the splat thickness during splat spreading and solidification.

3.5 Phase Development with Heat Treatment

Table 4 summarizes the weight percent concentrations of the coating phases following heat treatment, along with the goodness-of-fit (GofF) parameters from the Rietveld fitting using the MAUD software. Errors are presented for the parameters that were refined by the software program. The data were normalized for the phases: Cr_3C_2 , Cr_7C_3 ,

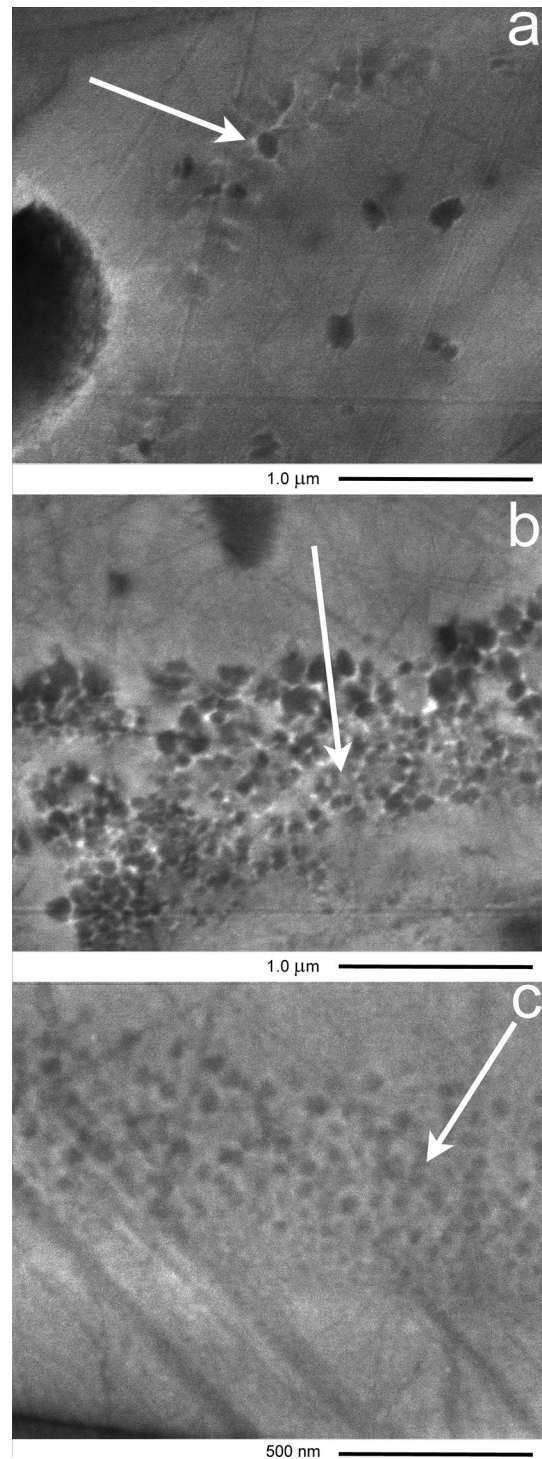


Fig. 12 High-magnification cross-sectional BSE images showing the breakup of the supersaturated Ni phase into two separate phases of bright- and dark-grayscale contrast (indicated by the arrows)

and the Ni alloy (i.e., the Cr_2O_3 content was excluded) prior to plotting the data in Fig. 13 and 14.

3.5.1 Mach II Ar- H_2 Trials. Heat treatment generated a dramatic change in the coating composition from the metastable state in the as-sprayed coatings to a more

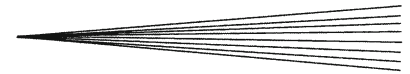


Table 4 Results from the Rietveld analysis for the heat-treated coatings

| Trial number/description | Spray distance, mm | Concentration, wt. % | | | | R value | Rw, % | Goff (sigma) |
|----------------------------------|--------------------|----------------------|--------------------------------|--------------------------------|--------------------------------|---------|-------|--------------|
| | | Ni (Cryst) | Cr ₂ O ₃ | Cr ₃ C ₂ | Cr ₇ C ₃ | | | |
| CD01 Ar-H ₂ low flow | 100 | 15.0 (±1.0) | 7.1 (±0.4) | 71.6 (±3.8) | 6.3 | 3.87 | 1.61 | |
| | 120 | 16.8 (±1.1) | 7.1 (±0.5) | 71.5 (±4.7) | 4.7 | 4.31 | 1.63 | |
| CD02 Ar-H ₂ high flow | 100 | 18.2 (±0.5) | 12.5 (±0.4) | 69.3 (±1.7) | 0.0 | 4.01 | 1.77 | |
| | 120 | 18.3 (±0.5) | 11.2 (±0.4) | 70.6 (±2.1) | 0.0 | 4.1 | 1.84 | |
| CD03 Ar-H ₂ low flow | 100 | 13.9 (±2.5) | 5.7 (±1.0) | 78.8 (±13.7) | 1.6 | 3.82 | 1.55 | |
| | 120 | 14.9 (±0.9) | 5.7 (±1.0) | 73.1 (±3.9) | 6.3 | 3.94 | 1.61 | |
| CD04 Ar-H ₂ high flow | 100 | 13.7 (±1.1) | 4.0 (±2.3) | 82.0 (±5.1) | 0.3 | 3.87 | 3.99 | |
| | 120 | 12.9 (±1.3) | 5.8 (±0.6) | 78.7 (±7.9) | 2.7 | 4.25 | 1.72 | |
| CD05 Ar-He | 80 | 13.7 (±0.6) | 9.4 (±0.4) | 59.4 (±1.8) | 17.5 | 4.08 | 1.66 | |
| | 100 | 13.4 (±0.5) | 9.3 (±0.4) | 53.6 (±1.5) | 23.7 | 4.78 | 1.73 | |
| | 120 | 11.9 (±0.3) | 9.8 (±0.4) | 45.6 (±1.0) | 32.7 | 4.81 | 1.97 | |
| CD06 Ar-H ₂ | 80 | 13.2 (±0.3) | 6.9 (±0.2) | 53.9 (±1.2) | 26.1 | 4.52 | 1.9 | |
| | 100 | 10.8 (±0.3) | 7.1 (±0.2) | 34.8 (±0.8) | 47.3 | 5.86 | 2.11 | |
| | 120 | 9.9 (±0.3) | 7.3 (±0.2) | 25.9 (±0.8) | 56.9 | 5.66 | 2.32 | |
| CD07 Ar-He | 80 | 15.0 (±1.2) | 6.9 (±0.5) | 74.7 (±5.7) | 3.4 | 3.66 | 1.51 | |
| | 100 | 15.3 (±1.0) | 6.7 (±0.4) | 73.5 (±4.8) | 4.4 | 4.15 | 1.49 | |
| | 120 | 14.1 (±0.5) | 7.9 (±0.4) | 63.7 (±1.8) | 14.3 | 3.94 | 1.63 | |
| CD08 Ar-H ₂ | 80 | 15.7 (±1.0) | 6.2 (±0.4) | 72.9 (±4.3) | 5.2 | 3.93 | 1.61 | |
| | 100 | 15.7 (±1.0) | 7.0 (±0.4) | 69.4 (±3.4) | 7.8 | 5.14 | 2.11 | |
| | 120 | 11.7 (±0.4) | 6.2 (±0.2) | 50.3 (±1.2) | 31.8 | 4.73 | 1.91 | |

equilibrium composition with heat treatment. The composition results were remarkably consistent between the low flow and high flow parameters in both the unshrouded and shrouded trials, Fig. 13. Cr₃C₂ dominated the coating composition. The Cr₇C₃ content was significantly reduced to only minor levels with heat treatment, emphasizing the metastable nature of this phase in the as-sprayed coatings. The composition of this phase also moved toward equilibrium based on the shift in peak position, implying a reduction in the dissolved Ni content.

Shrouding resulted in a higher equilibrium Cr₃C₂ content in both trials, which is assumed to result from the higher retained carbon content. The Ni alloy content reduced in concentration as the supersaturated amorphous material in the as-sprayed coating recrystallized and moved to a more equilibrium composition. The crystalline Ni alloy content was comparable to that in the starting powder of 15 wt.%. The results were comparable at both spray distances, which reflected the minimal changes observed in the other coating characteristics between 100 and 120 mm.

3.5.2 Subsonic Ar-He and Ar-H₂ Trials. The equilibrium composition of the subsonic anode nozzle coating showed a more dramatic variation as a function of spray distance than seen in the Mach II trials, Fig. 14. The equilibrium Cr₃C₂ content dramatically increased from that in the as-sprayed coatings but did not reach the equilibrium concentrations achieved in the Mach II trials. Furthermore, the Cr₃C₂ content decreased with increasing spray distance for both plasma compositions. Both these responses are assumed to result from the increase in decarburization in the subsonic trials with increasing spray distance. The unshrouded trials showed a linear decrease in Cr₃C₂ content with increasing distance, with the rate of reduction higher in the Ar-H₂ trial. The Cr₃C₂ content was significantly higher in the shrouded trials relative to the

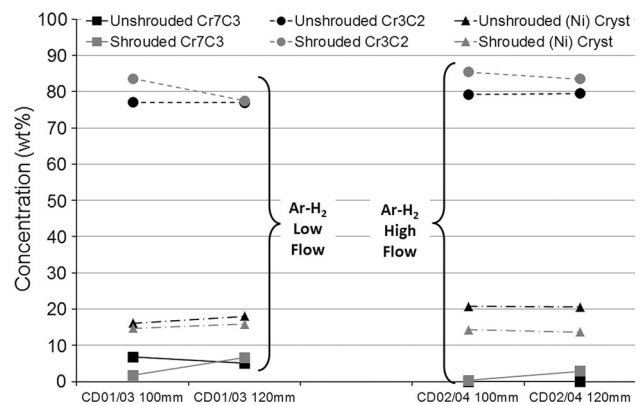


Fig. 13 Variation in the heat-treated coating composition as a function of spray distance for the unshrouded and shrouded Mach II nozzle trials CD01-CD04

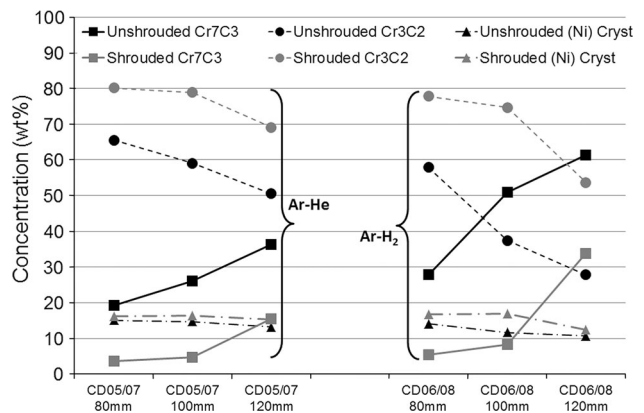


Fig. 14 Variation in the heat-treated coating composition as a function of spray distance for the unshrouded and shrouded subsonic nozzle trials CD05-CD08

unshrouded trials. Furthermore, the variation with spray distance showed a distinct trend for both plasma compositions—a slight reduction in concentration from 80 to 100 mm, followed by a much greater reduction in concentration from 100 to 120 mm. These trends were mirrored in the Cr_7C_3 concentration profiles—a linear increase in concentration with spray distance in the unshrouded trials, and a slight increase in concentration from 80 to 100 mm followed by a significant increase in concentration from 100 to 120 mm in the shrouded trials. In both plasmas, the Cr_7C_3 content was dramatically reduced in the shrouded trials. The crystalline Ni alloy contents in all the trials were comparable to those in the Mach II coatings and the starting powder, and showed minimal changes with spray distance.

The variation in the carbide composition with spray distance is assumed to result from the variation in carbon content. The approximately linear increase in Cr_7C_3 in the unshrouded trials is attributed to a constant rate of decarburization over the 80-120 mm range in spray distance. The unshrouded plasma is expected to have already entrained significant quantities of air prior to 80 mm (Ref 34-36), and so a too low oxygen concentration in the plasma is not expected to be a limiting factor in the degree of decarburization over this spray distance range. Decarburization increased with spray distance due to the longer exposure time of the particle to the oxidizing atmosphere.

In the shrouded trials, the same plasma parameters and carrier gas flows were used as in the unshrouded trials and so comparable particle trajectories through the plasma plume are assumed to have occurred. The variation in decarburization with spray distance from the unshrouded trial, therefore, suggests a variation in the oxygen concentration with spray distance. The results suggest that the gas shroud was effective in reducing the oxygen concentration out to 100 mm, but beyond that, significant air entrainment occurred. This protective effect was seen in both the Ar-He and Ar- H_2 plasma-sprayed coatings, in spite of the variations in particle temperature and velocity as a function of the plasma composition. A contributing factor to this response is the particle trajectories, which pass further away from the plasma centerline with increasing distance (Ref 9). This also brings into effect the radial oxygen content distribution as a function of spray distance.

Characterization of the microstructural changes in the coatings with heat treatment for such a large sample set was beyond the scope of this article. However, work is underway to characterize in detail the development in the carbide microstructure as a function of heat treatment time and temperature for several coatings using the plasma parameter sets from this work.

3.5.3 Analysis of the Crystalline Ni Alloy Composition. The transformation of the amorphous Ni alloy material in the as-sprayed coating to the crystalline Ni alloy in the heat-treated coating resulted in a dramatic reduction in the Cr concentration in solid solution from approximately 45-50 wt.%, Fig. 8, to less than 16 wt.%, Fig. 15. However, the Cr concentration in the Ni alloy in the coatings remained significantly higher than the 8 wt.%

value based on the Ni peak position in the powder XRD pattern. In the subsonic anode trials, the alloy Cr content was higher in the unshrouded trials for both plasma compositions. In addition, the Cr contents in the subsonic trials were higher than in the Mach II trials. These results suggest that the Ni alloy Cr content in the heat-treated coatings increased with increasing degrees of indicative carbon loss from the coating. This hypothesis is supported by the trends in Fig. 16 which plots the variation in the crystalline Ni alloy Cr content and the Cr_7C_3 concentration in the heat-treated coatings as a function of the indicative carbon loss for all of the results in this work (the results from Trial CD02 deviated considerably from the trends of all the other coatings and were considered outliers. For the sake of clarity, the results of this trial were omitted from the graph to better illustrate the general trends across the majority of the coatings). There is a linear increase in the Ni alloy Cr content with increasing carbon loss. However, this occurs in conjunction with a more complex trend in the development of the Cr_7C_3 phase with carbon loss. Carbon loss does, therefore, not

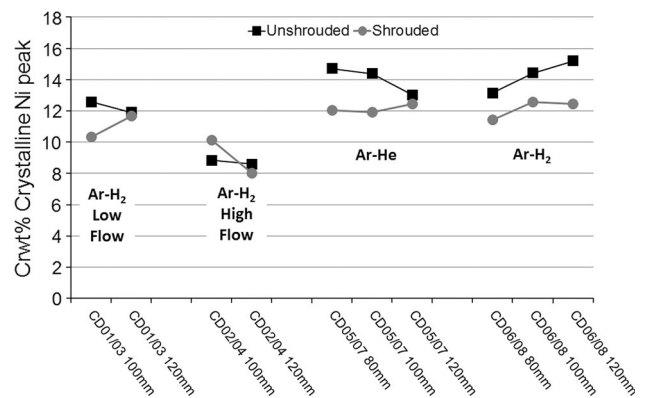


Fig. 15 Variation in the Cr concentration in the crystalline Ni alloy peak in the heat-treated coatings from trials CD01-CD08 as a function of spray distance

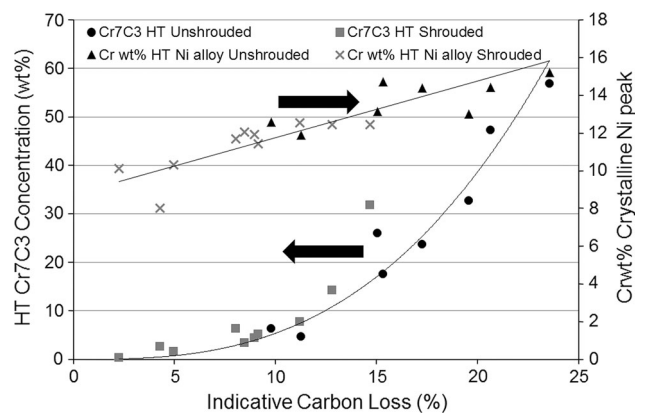


Fig. 16 Variation in the Cr_7C_3 concentration and Ni alloy Cr concentration in the heat-treated coatings as a function of indicative carbon loss for the unshrouded and shrouded trials

simply result in a linear increase in the Cr_7C_3 content as may have been expected. At low levels of carbon loss, Cr_7C_3 formation is low, but there is a notable increase in the Ni alloy Cr content. This result suggests that Cr_7C_3 formation does not occur preferentially. Otherwise, the Cr_7C_3 content would be expected to be higher, and the Ni alloy Cr content remains constant with increasing carbon loss. At high levels of carbon loss, the Ni alloy Cr content continues to increase, but the rate of Cr_7C_3 development increases significantly faster. This result points to a complex relationship between the equilibrium thermodynamics of Ni-Cr alloying and Cr_7C_3 formation as a function of carbon content.

3.5.4 Metastable Cr_7C_3 Development. In the as-sprayed coatings, solidification of the molten material in the splats is postulated to form a mixture of an Ni-based amorphous phase and a metastable Cr_7C_3 -based phase. This metastable Cr_7C_3 phase formed a significant, if not dominant, phase in the as-sprayed coatings and, hence, is expected to play a significant role in determining the coating properties. In the mechanism proposed in the analysis of the as-sprayed coating composition, the Ni amorphous phase formed preferentially, with the metastable phase forming from the excess Cr and C elements that could not be dissolved in the Ni alloy solid solution. According to this mechanism, increasing degrees of carbide dissolution, seen as decreasing concentrations of carbide, should show a direct increase in the metastable Cr_7C_3 content. In Fig. 17(a), the metastable Cr_7C_3 content in the as-sprayed coating is plotted as a function of the as-sprayed coating carbide content measured by image analysis. While there is a general trend of increasing metastable Cr_7C_3 content with decreasing carbide content (i.e., increasing degrees of carbide dissolution), there is a lot of spread in the data, with a broad range of Cr_7C_3 concentrations formed at each carbide concentration. Therefore, the coating carbide content based on image analysis is a weak indicator of the metastable Cr_7C_3 content in the coating. The results of the shrouded coatings tended to fall below those of the unshrouded coatings for a given coating carbide content, suggesting some dependence on the degree of carbon loss. In Fig. 17(b), the metastable Cr_7C_3 content in the as-sprayed coating is plotted as a function of the indicative carbon loss. The results show a gradual increase in the metastable Cr_7C_3 content with increasing indicative carbon loss. Significantly, this trend is consistent across both the unshrouded and shrouded coatings. This result suggests that for coatings which undergo high degrees of carbide dissolution, the degree of carbon loss is a better measure of the amount of metastable Cr_7C_3 that forms in the as-sprayed coating.

With heat treatment, the metastable Cr_7C_3 phase transformed into crystalline Cr_3C_2 and low concentrations of crystalline equilibrium Cr_7C_3 . In this regard, it would be of interest to know if any features of the as-sprayed coating could be used as indicators of how much equilibrium Cr_7C_3 forms after extended exposure at high temperature, and by default how much of the original Cr_3C_2 phase would be recovered. Figure 18(a) plots the crystalline Cr_7C_3 content in the heat-treated coating as a function

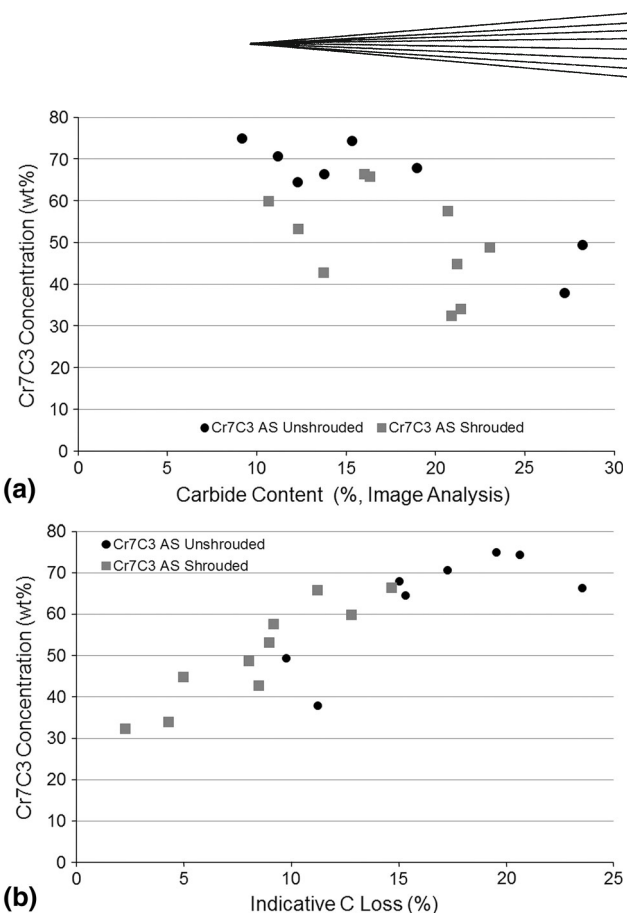


Fig. 17 Variation in the as-sprayed Cr_7C_3 concentration as a function of carbide content (a) and as a function of indicative carbon loss (b) for the unshrouded and shrouded trials

of the metastable Cr_7C_3 content in the as-sprayed coating. The dramatic reduction in Cr_7C_3 content with heat treatment is clearly highlighted in this figure. The magnitude of this reduction in Cr_7C_3 content is related to the amount of metastable Cr_7C_3 formed in the as-sprayed coating, but this relationship is complex. Furthermore, the spread in data for a given value of the as-sprayed metastable Cr_7C_3 content increases significantly with increasing metastable Cr_7C_3 content. This makes the metastable Cr_7C_3 content in the as-sprayed coating a poor indicator for the quantity of equilibrium crystalline Cr_7C_3 that forms with heat treatment.

In Fig. 18(b), the crystalline Cr_7C_3 content in the heat-treated coating is plotted as a function of the carbide content in the as-sprayed coatings based on image analysis. The results indicate that the as-sprayed carbide content is also a poor indicator of the Cr_7C_3 content that will form with heat treatment. For both the shrouded and unshrouded trials, the data are very spread and notably dependent upon the specific spray parameters used in each trial.

Figure 16 plots the variation in crystalline Cr_7C_3 content in the heat-treated coatings as a function of the indicative carbon loss. The indicative carbon loss again appears to be a better measure of the amount of Cr_7C_3 that will form with heat treatment, although the relationship between these two properties is complex. It should also be noted that the Cr_7C_3 content and the carbon loss

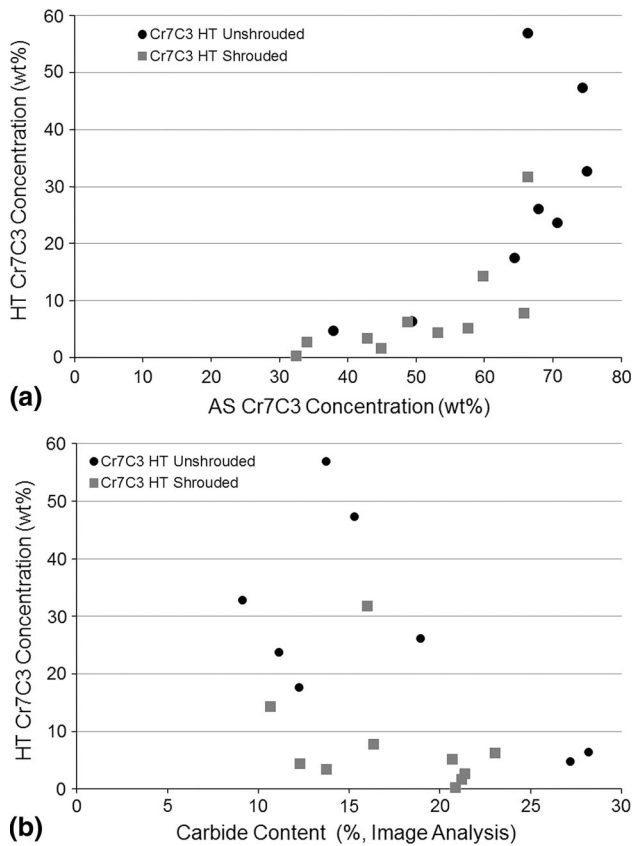


Fig. 18 Variation in the Cr₇C₃ concentration in the heat-treated coatings as a function of the Cr₇C₃ concentration in the as-sprayed coatings (a) and as a function of the as-sprayed carbide content (b) for the unshrouded and shrouded trials

results were generated from the same XRD data. Additional trials with independently verified carbon loss results (e.g., from a LECO combustion analysis) are required to confirm this response.

4. Conclusions

The aim of Part 2 of this two-part article series was to characterize the effect of spray distance on the compositional development in high-energy plasma-sprayed Cr₃C₂-NiCr coatings. Trials were sprayed using low-velocity and high-velocity anode nozzle configurations, over the spray distance range 80-120 mm. Two shroud configurations were investigated (a solid conical coaxial shroud in the high-velocity trials, and a coaxial cylindrical gas shroud in the subsonic trials), and the results contrasted with the unshrouded trials. The key conclusions from this work are

- Four phases were identified in the XRD analysis—a crystalline Cr₃C₂ phase, a crystalline Ni alloy phase, an amorphous/nano-crystalline Ni alloy phase, and a metastable (Cr,Ni)₇C₃ phase. The metastability of the latter was based on the marked reduction in intensity of this phase with heat treatment and the shift in peak positions toward those of equilibrium Cr₇C₃.

- In the low flow rate Ar-H₂ Mach II anode nozzle trials, shrouding decreased the coating Cr₃C₂ content at 100 mm, indicating an increase in the degree of carbide dissolution. The metastable Cr₇C₃ phase dominated the coating composition in both the unshrouded and shrouded trials but showed contrasting trends with spray distance.
- In the high flow rate Ar-H₂ Mach II anode nozzle trials, shrouding generated a dramatic decrease in the coating Cr₃C₂ content at 100 mm. This was accompanied by a significant increase in the metastable Cr₇C₃ content. The amorphous Ni alloy content remained comparable in both the unshrouded and shrouded trials, in spite of the carbide content variation. No significant change in coating composition occurred with the increase in spray distance.
- In the subsonic nozzle trials, the degree of Cr₃C₂ dissolution decreased with the use of shrouding in the Ar-He trial at 80 mm, but in Ar-H₂ trials, the Cr₃C₂ content was comparable with and without shrouding at this distance. With increasing spray distance, the Cr₃C₂ content decreased in all trials, indicative of increasing carbide dissolution with the longer exposure time in the plasma. The amorphous Ni alloy content was consistently lower in the unshrouded trials for both plasma compositions and tended to decrease with increasing spray distance. The metastable Cr₇C₃ phase dominated the composition of all the subsonic anode coatings and increased in concentration with increasing spray distance. The unshrouded trials formed consistently higher concentrations of this phase than the shrouded trials for both plasmas.
- Cooling of the particles in-flight leads to precipitation of carbides onto retained Cr₃C₂ grains as well as forming independent acicular particles. More generally, rapid solidification transformed the Cr- and C-saturated Ni alloy liquid into regions of amorphous/nano-crystalline solid material of varying grayscale contrast. High-magnification BSE imaging indicated that regions which appeared to be homogeneous at low magnification were composed of two phases with structures on the < 100 nm scale. These were postulated to account for the amorphous Ni alloy and metastable Cr₇C₃ phases which dominated the coating composition.
- The degree of indicative carbon loss was found to be a better measure of the extent of metastable Cr₇C₃ formation in the as-sprayed coatings and Cr₇C₃ formation in the heat-treated coatings, than the retained carbide content.

Acknowledgments

The author gratefully acknowledges the support of Associate Professor Brian Gabbitas and the University of Waikato for their collaboration in the development and manufacture of the shrouds and for allowing their use in this work. The assistance of Holster Engineering in per-



forming the spray trials is sincerely appreciated. The support in the preparation and analysis of the coatings provided by the Department of Chemical and Materials Engineering at the University of Auckland is also gratefully appreciated. Funding for this work was provided by the Marsden Fund Council from New Zealand Government funding, administered by the Royal Society of New Zealand.

References

1. L.-M. Berger, Hardmetals as Thermal Spray Coatings, *Powder Metall.*, 2007, **50**(3), p 205-214
2. S. Matthews, B. James, and M. Hyland, The Role of Microstructure in the High Velocity Erosion of Cr₃C₂-NiCr Thermal Spray Coatings: Part 1—As-Sprayed Coatings, *Surf. Coat. Technol.*, 2009, **203**, p 1086-1093
3. F. Otsubo, H. Era, T. Uchida, and K. Kishitake, Properties of Cr₃C₂-NiCr Cermet Coating Sprayed by High Power Plasma and High Velocity Oxy-fuel Processes, *J. Therm. Spray Technol.*, 2000, **9**(4), p 499-504
4. D. Poirier, J.-G. Legoux, and R. Lima, Engineering HVOF-Sprayed Cr₃C₂-NiCr Coatings: The Effect of Particle Morphology and Spraying Parameters on the Microstructure, Properties and High Temperature Wear Performance, *J. Therm. Spray Technol.*, 2013, **22**(2-3), p 280-289
5. S. Zimmermann and H. Kreye, Chromium Carbide Coatings Produced with Various HVOF Spray Systems, *Thermal Spray: Practical Solutions for Engineering Problems*, C.C. Berndt, Ed., ASM International, Novlety, 1996, p 147-152
6. S. Matthews, "Erosion-Corrosion of Cr₃C₂-NiCr High Velocity Thermal Spray Coatings," Ph.D. Thesis, Department of Chemical and Materials Engineering, The University of Auckland, 2004
7. S. Matthews, M. Hyland, and B. James, Long-Term Carbide Development in High Velocity Oxygen Fuel/High Velocity Air Fuel Cr₃C₂-NiCr Coatings Heat Treated at 900°C, *J. Therm. Spray Technol.*, 2004, **13**(4), p 526-536
8. S. Matthews, Development of High Carbide Dissolution/Low Carbon Loss Cr₃C₂-NiCr Coatings by Shrouded Plasma Spraying, *Surf. Coat. Technol.*, 2014, **258**, p 886-900
9. S. Matthews, Carbide Dissolution/Carbon Loss as a function of Spray Distance in Unshrouded/Shrouded Plasma Sprayed Cr₃C₂-NiCr Coatings, *J. Therm. Spray Technol.*, 2014, doi:10.1007/s11666-014-0210-2
10. E. Bouzy, G. le Caer, and E. Bauer-Grosse, New Metastable Carbides Produced by Crystallization of Amorphous CrC Alloys, *Mater. Sci. Eng., A*, 1991, **133**(C), p 640-643
11. L. He, Hexagonal Close-Packed Nickel or Ni₃C?, *J. Magn. Magn. Mater.*, 2010, **322**(14), p 1991-1993
12. A. Inoue and T. Masumoto, Formation of Nonequilibrium Cr₃C Carbide in CrC Binary Alloys Quenched Rapidly from the Melt, *Scr. Metall.*, 1979, **13**(8), p 711-715
13. A. Inoue, S. Sakai, H. Kimura, and T. Masumoto, Crystallization Temperature and Hardness of New Chromium-Based Amorphous Alloys, *Trans. Jpn. Inst. Met.*, 1979, **20**(5), p 255-262
14. S. Loubière, C. Laurent, J.P. Bonino, and A. Rousset, A Metastable Chromium Carbide Powder Obtained by Carburization of a Metastable Chromium Oxide, *J. Alloy. Compd.*, 1996, **243**(1-2), p 59-66
15. P. Nash, The Cr-Ni (Chromium-Nickel) System, *Bull. Alloy Phase Diagrams*, 1986, **7**(5), p 466-476
16. Z.L. Schaefer, K.M. Weeber, R. Misra, P. Schiffer, and R.E. Schaak, Bridging hcp-Ni and Ni 3C Via a Ni 3C 1-x Solid Solution: Tunable Composition and Magnetism in Colloidal Nickel Carbide Nanoparticles, *Chem. Mater.*, 2011, **23**(9), p 2475-2480
17. R. Sinclair, T. Itoh, and R. Chin, In Situ TEM Studies of Metal-Carbon Reactions, *Microsc. Microanal.*, 2002, **8**(4), p 288-304
18. M. Singleton and P. Nash, The C-Ni (Carbon-Nickel) System, *Bull. Alloy Phase Diagrams*, 1989, **10**(2), p 121-126
19. T.Y. Velikanova, A.A. Bondar, and A.V. Grytsiv, Chromium-Nickel-Carbon (Cr-Ni-C) Phase Diagram, *J. Phase Equilib.*, 1999, **20**(2), p 125-147
20. M. Venkatraman and J.P. Neumann, The C-Cr (Carbon-Chromium) System, *Bull. Alloy Phase Diagrams*, 1990, **11**(2), p 152-159
21. B.J. Lee, On the Stability of Cr Carbides, *Calphad*, 1992, **16**(2), p 121-149
22. D.Y. Kim, M.S. Han, and J.G. Youn, Characterisation of Erosion Resistant Cr₃C₂-NiCr Plasma Sprayed Coatings, *Practical Solutions for Engineering Problems—Proceedings of the 9th National Thermal Spray Conference*, C.C. Berndt, Ed., ASM International, 1996, p. 123-128
23. S.R. Nishitani, K.N. Ishihara, R.O. Suzuki, and P.H. Shingu, Metastable Solid Solubility Limit of Carbon in the Ni-C System, *J. Mater. Sci. Lett.*, 1985, **4**(7), p 872-875
24. T. Tanaka, K.N. Ishihara, and P.H. Shingu, Formation of Metastable Phases of Ni-C, *Metall. Trans. A*, 1992, **23**(9), p 2431-2435
25. J.K. Chen, D. Farkas, and W.T. Reynolds, Jr., Atomistic Simulation of an f.c.c./b.c.c Interface in Ni-Cr Alloys, *Acta Mater.*, 1997, **45**(11), p 4415-4421
26. A.A. Bondar, V.A. Maslyuk, T.Y. Velikanova, and A.V. Grytsiv, Phase Equilibria in the Cr-Ni-C System and Their Use for Developing Physicochemical Principles for Design of Hard Alloys Based on Chromium Carbide, *Powder Metall. Met. Ceram.*, 1997, **36**(5-6), p 242-252
27. S. Matthews, Shrouded Plasma Spray of Ni-20Cr Coatings Utilizing Internal Shroud Film Cooling, *Surf. Coat. Technol.*, 2014, **249**, p 56-74
28. L. Lutterotti, Total Pattern Fitting for the Combined Size-Stress-Texture Determination in Thin Film Diffraction, *Nuclear Inst. Methods Phys. Res.*, 2010, **2**(268), p 334-340
29. M.H. Staia, M. Suárez, D. Chicot, J. Lesage, A. Iost, and E.S. Puchi-Cabrera, Cr₃C₂-NiCr VPS Thermal Spray Coatings as Candidate for Chromium Replacement, *Surf. Coat. Technol.*, 2013, **220**, p 225-231
30. B.D. Cullity, *Elements of X-ray Diffraction*, 2nd ed., Addison-Wesley Publishing Company, Inc, Reading, 1978
31. S. Graulis, D. Chateigner, R.T. Downs, A.F.T. Yokochi, M. Quirós, L. Lutterotti, E. Manakova, J. Butkus, P. Moeck, and A. Le Bail, Crystallography Open Database—An open-access collection of crystal structures, *J. Appl. Crystallogr.*, 2009, **42**(4), p 726-729
32. L. Lutterotti, R. Ceccato, R. Dal Maschio, and E. Pagani, Quantitative Analysis of Silicate Glass in Ceramic Materials by the Rietveld Method, *Mater. Sci. Forum*, 1998, **278**, p 87-92
33. S. Sampath and H. Herman, Rapid Solidification and Microstructure Development During Plasma Spray Deposition, *J. Therm. Spray Technol.*, 1996, **5**(4), p 445-456
34. G. Espie, A. Denoirjean, P. Fauchais, J.C. Labbe, J. Dubsy, O. Schneeweiss, and K. Volenik, In-Flight Oxidation of Iron Particles Sprayed Using Gas and Water Stabilized Plasma Torch, *Surf. Coat. Technol.*, 2005, **195**, p 17-28
35. J.R. Fincke, W.D. Swank, and D.C. Haggard, Entrainment and demixing in subsonic argon/helium thermal plasma jets, *Proceedings of the 1993 National Thermal Spray Conference*, 1993, p. 49-54
36. R.A. Neiser, M.F. Smith, and R.C. Dykhuizen, Oxidation in Wire HVOF-Sprayed Steel, *J. Therm. Spray Technol.*, 1998, **7**(4), p 537-545